Report No.
UCB/SEMM-2023/01

Structural Engineering
Mechanics and Materials

Finite element modeling of viscoelastic liquid crystal elastomers

By

Ali El Hajj Chehade, Beijun Shen,
Chris M. Yakacki, Thao D. Nguyen, Sanjay Govindjee

December 2023

Department of Civil and Environmental Engineering
University of California, Berkeley

Finite element modeling of viscoelastic liquid crystal elastomers

Ali El Hajj Chehade[*], Beijun Shen[†], Chris M. Yakacki[‡], Thao D. Nguyen[§], Sanjay Govindjee[¶]

December 21, 2023

Abstract

Liquid crystal elastomers (LCEs) are elastomeric networks with anisotropic monomers that reorient in response to applied loads, and in particular, thermomechanical loads. LCE complex microstructures translate into complex behaviors, such as soft elasticity, rate-dependency, and hysteresis. In this work, we developed a three-dimensional finite element implementation for monodomain LCEs, with the material modeled as a finite deformation viscoelastic network with a viscous director. The formulation is designed so that the director field can be modeled as an internal variable. Unique to this class of materials is that their deformation response function depends on the full deformation gradient and not just the right-stretch tensor. This results in the material tangent losing its 'usual' symmetry properties. Accordingly, this makes the use of a first Piola-Kirchhoff finite element formulation advantageous. We utilize this framework to examine a number of nuances associated with the simulation and design of LCE based systems. In particular, we investigate in some detail the importance of a careful characterization of an LCE's initial director field. Via simulations of separate tension and compression experiments, we highlight the possibility of incorrect predictions when even small perturbations to initial conditions occur. The simulations are also used to illustrate the goodness of the model in replicating simple and complex experimental results, including the first-of-their-kind buckling-like column compression and thick-walled balloon inflation simulations.

[*]ali_elhajjchehade@berkeley.edu
[†]beijunshen@jhu.edu
[‡]chris.yakacki@ucdenver.edu
[§]vicky.nguyen@jhu.edu
[¶]Corresponding author, s_g@berkeley.edu

1 Introduction

Nematic liquid crystal elastomers (LCEs) are materials that exhibit a mixture of polymeric behavior and liquid crystalline behavior. They are crosslinked polymeric networks where the individual polymer chains are formed of stiff nematic liquid crystalline molecules. At low temperatures, the liquid crystal molecules align due to energetic effects, causing their corresponding chains to align in a dominant orientation called the director, resulting in an oriented macroscopic behavior. At higher temperatures, entropic effects dominate and the liquid crystal molecules randomly orient themselves, leading to random chain orientations and an overall isotropic state. Other types of liquid crystal ordering are possible (see e.g. Sonnet and Virga, 2012) but herein we only consider nematic LCEs. Furthermore, depending on whether the material was aligned during synthesis, the nematic network can form monodomain or polydomain microstructures. For this work, we focus on monodomain LCEs where the molecule/chain orientation at a continuum point can be represented by a single unit vector, i.e. the director.

The behavior described above is not too dissimilar from what is seen in strain-crystallizing elastomers (see e.g., Gent, 1954; Gaylord, 1976; Gaylord and Lohse, 1976; Toki et al., 2005; Mistry and Govindjee, 2014). However, LCEs also display the unique ability to re-orient the director at constant order. This leads to the defining mechanical feature of LCEs, which is without a doubt, soft elasticity. This phenomenon occurs when the material is subjected to stretching perpendicular to a uniform director field while localized shear strains are also kinematically permissible. In this setting, which occurs in simple uniaxial tension experiments, the material stretches with near-zero force as the director field rotates to align with the stretching direction. Only after the director field fully aligns with the load does the stress appreciably increase. The physics behind this phenomenon has been explained and well modelled using the so-called neo-classical free energy, first proposed by Bladon et al. (1993). Further developments in the elastic regime include the mathematical analysis papers of DeSimone and Dolzmann (2002) and Conti et al. (2002) who introduced the all-important quasi-convex relaxation of the neo-classical model; see also Warner and Terentjev (2003), Fried and Sellers (2004), and Agostiniani and DeSimone (2012), among others, for additional extensions of these models.

From a computational point of view for finite deformations, there are some works that investigate the thermomechanical properties of LCEs using finite elements – likely the first being the work of Conti et al. (2002) who applied the quasi-convexified version of the neo-classical model coupled with a stabilizing neo-Hookean energy within a finite element setting; it should be noted that this framework treats the material director in a non-explicit effective way. More recently, Zhang et al. (2019) formulated the governing equations for monodomain LCE boundary value problems using a Rayleigh dissipation function to account for viscous director and network evolution, similar to Sonnet and Virga (2012), and solved the governing equations using plane stress finite elements. We note, however, that LCEs possess viscoelastic behavior; they are not fluids (see Azoug et al., 2016; Linares et al., 2020). Though our focus is monodomain materials, we note that for polydomain materials, Lee et al. (2023) has recently

proposed a model with a viscously evolving microstructure coupled to a Kelvin-Voigt stress response, along with a finite element implementation for solving boundary value problems.

Astonishingly, aside from the torsion and bi-axial stretching examples in Lee et al. (2023), most of LCE finite element literature only simulates the tension of LCE samples (whose results can be predicted using simple material point calculations). Other works linearize the free energy models and are thus not applicable at the large deformations seen in experiments and applications. Further, most simulation works appear to use explicit time-stepping schemes (useful only for transient wave propagation situations) or do not use consistent algorithmic tangents, thus losing the quadratic convergence property of Newton's method, which is very desirable for quasi-static situations or those involving only structural level dynamics. Our aim here is to present in some detail a general-purpose monodomain viscoelastic LCE model and its finite element implementation for the purposes of solving complex three-dimensional boundary-value problems. Furthermore, our finite element formulation is aimed at implicit time integration and/or quasi-static problems and the proper attainment of quadratic convergence for computational efficiency. The choice of the stress measure and the frame over which the boundary value problem is formulated will also play an important role with respect to efficiency. In particular, we highlight the fact that it is more efficient to utilize an element formulated in the first Piola-Kirchhoff form when working with LCE material models.

We first present the theoretical framework and the continuum equations to be solved, closely following Wang et al. (2022). It is noted that this model incorporates viscous director rotation as well as *viscoelastic network response* and is built upon the equilibrium neo-classical concept and its generalization as developed in DeSimone and Teresi (2009). We detail the finite element formulation most well suited to these models and discuss the nuances of solving for the local stress updates. We then use our finite element implementation to study intricate issues associated with solving boundary value problems for LCE systems. In particular, we take up the fact that the pointwise initial director field can not be fully specified experimentally. Thus it must be interpreted as a stochastic field and this has paramount bearing on whether or not simulations produce physically representative responses. This is done for the common tension case, where we also consider the unloading process – something which is not normally seen in the literature. We follow this by considering what occurs in compression, again a case that is not often seen in the literature. Here we also consider comparisons to experimental data and conjecture the need for a nonlinear dependency of director viscosity on deformation. Our final example is the inflation of a cylindrical LCE balloon, an experiment conducted by He et al. (2020). The experiment demonstrates anomalous inflation behavior and the ability of the model and numerical algorithm to reproduce these behaviors.

2 Problem Statement

Monodomain nematic LCEs are materials that can be described by two global kinematic degrees of freedom. The first is the classical displacement field $\boldsymbol{u}$, while the second is a

director field $\boldsymbol{d}$ describing the microstructure of the material. However, for the class of problems we are interested in, the director may be treated as an internal variable as long as no director-conjugate actions are applied and director-gradient effects are omitted (see Wang et al. (2022) for technical details on these assumptions).

2.1 Governing equations

Given a macroscopic continuum body with reference configuration $\mathcal{B}$, its boundary $\partial\mathcal{B}$ may be split into two parts $\partial_u\mathcal{B}$ and $\partial_T\mathcal{B}$ where displacement boundary conditions and traction boundary conditions are specified respectively. The actions applied on the body consist of a body force (per unit mass) $\boldsymbol{B}$ in $\mathcal{B}$, a surface traction (per unit reference area) $\boldsymbol{T}$ on $\partial_T\mathcal{B}$, and an imposed motion $\bar{\boldsymbol{\varphi}}$ on $\partial_u\mathcal{B}$; see Fig. 1. The strong form of the governing equation, balance of linear momentum, reads

$$\mathrm{Div}[\mathbf{P}] + \boldsymbol{B} = \rho_0 \ddot{\boldsymbol{u}}\,, \tag{1}$$

where $\mathbf{P}$ is the first Piola-Kirchhoff stress, Div is the referential divergence operator, ρ_0 is the material density per unit reference volume, and $\boldsymbol{u}$ is the material displacement.

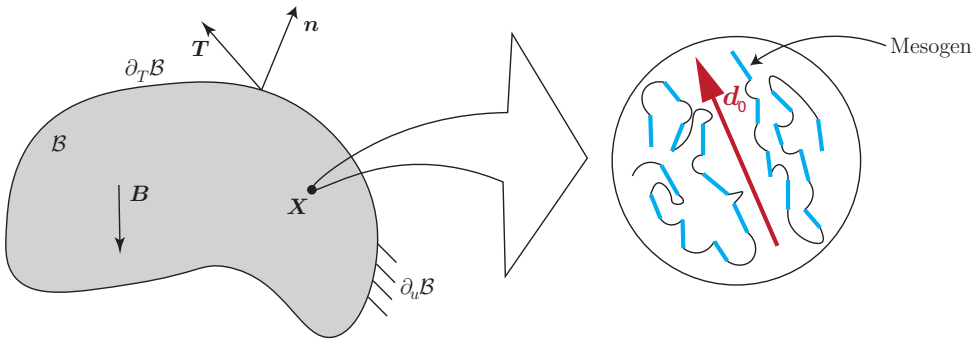

Figure 1: Reference body with imposed tractions and body forces. Material points are described by an initial director field $\boldsymbol{d}_0$ which represents the expected local orientation of liquid crystal mesogens (cyan lines) connected by flexible spacers (black curves).

We wish to solve the mechanical problem whose weak form statement is:

Find $\boldsymbol{\varphi} \in \mathcal{S} = \{\boldsymbol{\varphi}(\boldsymbol{X}) \mid \boldsymbol{\varphi}(\boldsymbol{X}) = \bar{\boldsymbol{\varphi}}(\boldsymbol{X}) \text{ for } \boldsymbol{X} \in \partial_u\mathcal{B}\}$ such that

$$\int_{\mathcal{B}} [\mathbf{P} : \mathrm{Grad}\,\delta\boldsymbol{\varphi} + \rho_0 \ddot{\boldsymbol{u}} \cdot \delta\boldsymbol{\varphi}]\; dV = \int_{\mathcal{B}} \rho_0 \boldsymbol{B} \cdot \delta\boldsymbol{\varphi}\, dV + \int_{\partial_T\mathcal{B}} \boldsymbol{T} \cdot \delta\boldsymbol{\varphi}\, dA \qquad \forall\, \delta\boldsymbol{\varphi} \in \mathcal{V}\,, \tag{2}$$

where $\delta\boldsymbol{\varphi}$ is a function in the set of admissible variations $\mathcal{V} = \{\delta\boldsymbol{\varphi}(\boldsymbol{X}) \mid \delta\boldsymbol{\varphi}(\boldsymbol{X}) = \boldsymbol{0} \text{ for } \boldsymbol{X} \in \partial_u\mathcal{B}\}$. All functions in $\mathcal{V}$ and $\mathcal{S}$ are assumed to be properly weakly differentiable in $\mathcal{B}$.

The weak form (2) will be used to compute the incremental solutions in a time/load stepping procedure. Due to the peculiarities of LCE models, we present a finite element formulation

directly in first Piola-Kirchhoff form, as it presents some simplifying advantages – especially considering that LCE free energies can not be strictly written in terms of symmetric deformation measures, such as the right and left Cauchy-Green deformation tensors. The first Piola-Kirchhoff form is also noted to be necessary for the case of LCE models that incorporate director gradient effects (something that we do not explicitly consider in this work).

2.2 The Constitutive Equations

In the model of Wang et al. (2022), which we use here, the viscoelasticity of the network is introduced by the Sidoroff (1974) multiplicative kinematic split of the deformation gradient into an elastic part and a viscous part:

$$\mathbf{F} = \mathbf{F}^{e(k)}\mathbf{F}^{v(k)} \qquad k = 1, \ldots, N\,, \tag{3}$$

where one can allow for multiple (N) viscoelastic relaxation mechanisms. In what follows, we consider only the single relaxation case to keep the presentation as simple as possible, and thus we drop the superscript (k) without loss of generality.

Accompanying (3) is the additive split of the free energy into an equilibrium part and a non-equilibrium part (similar to a standard linear solid):

$$\Psi\left(\mathbf{F}, \mathbf{F}^e, \boldsymbol{d}\right) = \Psi_{eq}\left(\mathbf{F}, \boldsymbol{d}\right) + \Psi_{neq}\left(\mathbf{F}^e, \boldsymbol{d}\right)\,. \tag{4}$$

The evolution of the internal state is governed by a set of coupled ordinary differential equations:

$$\dot{\mathbf{F}}^v = \frac{1}{\eta_N}\left(\mathbf{F}^e\right)^\top \frac{\partial \Psi_{neq}}{\partial \mathbf{F}^e}\left(\mathbf{F}^e, \boldsymbol{d}\right)\mathbf{F}^v\,, \tag{5}$$

$$\dot{\boldsymbol{d}} = \mathbf{W}\boldsymbol{d} - \frac{1}{\eta_D}\left(\mathbf{1} - \boldsymbol{d}\otimes\boldsymbol{d}\right)\frac{\partial \Psi}{\partial \boldsymbol{d}}\left(\mathbf{F}, \mathbf{F}^e, \boldsymbol{d}\right)\,, \tag{6}$$

where $\eta_N > 0$ and $\eta_D > 0$ are the network and director viscosities respectively, and $\mathbf{W}$ is the skew part of the spatial velocity gradient. Note that (5) and (6) satisfy the physical requirements of frame invariance and non-negative entropy production. The first Piola-Kirchhoff stress in this model is given by the relation

$$\mathbf{P} = \mathrm{sym}\left(\frac{\partial \Psi_{eq}}{\partial \mathbf{F}}\left(\mathbf{F}, \boldsymbol{d}\right)\mathbf{F}^\top + \frac{\partial \Psi_{neq}}{\partial \mathbf{F}^e}\left(\mathbf{F}^e, \boldsymbol{d}\right)\left(\mathbf{F}^e\right)^\top\right)\mathbf{F}^{-\top}\,. \tag{7}$$

Remark 1. The concrete forms that we will later use for Ψ_{eq} and Ψ_{neq} are the neo-classical

$$\Psi_{NC}\left(\mathbf{F}, \boldsymbol{d}\right) = \mu\Psi_1\left(I_N\right) - \mu\log J + \Lambda\, U\left(J\right) \tag{8}$$

and neo-Gent

$$\Psi_{NG}\left(\mathbf{F}, \boldsymbol{d}\right) = \mu\Psi_2\left(I_N; J_m\right) - \mu\log J + \Lambda\, U\left(J\right)\,. \tag{9}$$

models. Here,

$$\Psi_1(I) = \frac{1}{2} I\,, \tag{10}$$

$$\Psi_2(I; J_m) = -\frac{J_m}{2} \log\left(1 - \frac{I-3}{J_m}\right)\,, \tag{11}$$

the (small deformation) shear and Lamé moduli are μ and Λ, respectively, $J = \det \mathbf{F}$, J_m is the Gent locking parameter, $U(J) = \left(J^2 - 1 - 2\log J\right)/4$, $I_N = \operatorname{tr}\left(\mathbf{F}\boldsymbol{l}_0\mathbf{F}^\top\boldsymbol{l}^{-1}\right)$, and the so-called step-length tensors are

$$\boldsymbol{l}_0 = \mathbf{1} + (r-1)\,\boldsymbol{d}_0 \otimes \boldsymbol{d}_0 \tag{12}$$

and

$$\boldsymbol{l}^{-1} = \mathbf{1} + \left(\frac{1}{r} - 1\right)\boldsymbol{d} \otimes \boldsymbol{d}\,. \tag{13}$$

In (12) and (13), the initial and current directors are $\boldsymbol{d}_0$ and $\boldsymbol{d}$ respectively and r is the anisotropy ratio that defines the degree of the orientation of the chains.

Remark 2. Considering only the equilibrium energies, it is noted that the dependence in the neo-classical or neo-Gent models upon their arguments is via the mixed invariants

$$\operatorname{tr}(\mathbf{F}^\top\mathbf{F}),\ \boldsymbol{d}\cdot\mathbf{b}\boldsymbol{d},\ \boldsymbol{d}_0\cdot\mathbf{C}\boldsymbol{d}_0,\ \text{and}\ \boldsymbol{d}\cdot\mathbf{F}\boldsymbol{d}_0, \tag{14}$$

where $\mathbf{b}$ and $\mathbf{C}$ are the left and right Cauchy-Green deformation tensors respectively. The presence of the last invariant implies that the rotation of the polar decomposition does not disappear as one sees in "ordinary" materials (e.g. hyperelastic materials).

Remark 3. It should be observed that $\boldsymbol{d}\cdot\mathbf{F}\boldsymbol{d}_0$ is frame invariant, since the director transforms under changes of observer frame as $\boldsymbol{d}^* = \boldsymbol{Q}\boldsymbol{d}$ and the deformation gradient as $\mathbf{F}^* = \boldsymbol{Q}\mathbf{F}$ for a given rotation $\boldsymbol{Q}$. However, the director field is independent of the deformation field and thus all of $\mathbf{F}$, not just the right-stretch, plays a role in the constitutive response.

3 Constitutive discretization

Given a solution to (2) at time t_n, the classic question is to find the solution to the same equation at time t_{n+1}. Accordingly, we must compute $\mathbf{P}_{n+1}$, the first Piola-Kirchhoff stress at t_{n+1}:

$$\mathbf{P}_{n+1} = \operatorname{sym}\left(\frac{\partial \Psi_{eq}}{\partial \mathbf{F}}\left(\mathbf{F}_{n+1}, \boldsymbol{d}_{n+1}\right)\mathbf{F}_{n+1}^\top + \frac{\partial \Psi_{neq}}{\partial \mathbf{F}^e}\left(\mathbf{F}^e_{n+1}, \boldsymbol{d}_{n+1}\right)\left(\mathbf{F}^e_{n+1}\right)^\top\right)\mathbf{F}_{n+1}^{-\top}\,. \tag{15}$$

In what follows, we omit discussion of the inertial term as its treatment is standard. Furthermore, to avoid congesting this section with definitions, some of the notation and symbols used are defined in Appendix A.

3.1 Constitutive evaluation

In order to compute the stress (15) and its derivative with respect to the current deformation gradient $\mathbf{F}_{n+1}$, the internal variables must be computed. In the standard strain-driven finite element setting, the current deformation gradient $\mathbf{F}_{n+1}$ (and the prior history) is known and the quantities of interest (at every Gauss point) are $\mathbf{P}_{n+1}$, $\mathbf{F}^e_{n+1}$, $\mathbf{F}^v_{n+1}$, and $\boldsymbol{d}_{n+1}$. This is done by applying a Backward Euler numerical scheme to (5) and (6):

$$\mathbf{F}^v_{n+1} - \mathbf{F}^v_n - \frac{\Delta t_n}{\eta_N} \left(\mathbf{F}^e_{n+1}\right)^\top \frac{\partial \Psi_{neq}}{\partial \mathbf{F}^e} \left(\mathbf{F}^e_{n+1}, \boldsymbol{d}_{n+1}\right) \mathbf{F}^v_{n+1} = \mathbf{0}\,, \tag{16}$$

$$\hat{\boldsymbol{d}}_{n+1} - \boldsymbol{d}_n - \Delta t_n \mathbf{W}_{n+1} \boldsymbol{d}_{n+1} + \frac{\Delta t_n}{\eta_D} \left(\mathbf{1} - \boldsymbol{d}_{n+1} \otimes \boldsymbol{d}_{n+1}\right) \frac{\partial \Psi}{\partial \boldsymbol{d}} \left(\mathbf{F}_{n+1}, \mathbf{F}^e_{n+1}, \boldsymbol{d}_{n+1}\right) = \mathbf{0}\,, \tag{17}$$

$$\hat{\boldsymbol{d}}_{n+1} - \boldsymbol{d}_{n+1} \left\|\hat{\boldsymbol{d}}_{n+1}\right\| = \mathbf{0}\,, \tag{18}$$

where Δt_n is the n^{th} time step size. Note that (6) is discretized into (17) where we have introduced $\hat{\boldsymbol{d}}_{n+1}$ as an intermediate un-normalized director to account for the fact that $\boldsymbol{d} \in S^2$, the unit sphere. Accordingly, we introduce (18) as a projection back onto S^2. The equations for the internal variables are nonlinear and are therefore solved using a local Newton-Raphson scheme at the Gauss point level.

3.1.1 Local nonlinear solution

Relations (16)-(18) together with the multiplicative split of the deformation gradient constitute 2 tensorial and 2 vectorial relations that must be solved for $\mathbf{F}^e_{n+1}$, $\mathbf{F}^v_{n+1}$, $\boldsymbol{d}_{n+1}$, and $\hat{\boldsymbol{d}}_{n+1}$, given $\mathbf{F}_{n+1}$ in a finite element setting. We collect these in a single residual $\boldsymbol{g}(\boldsymbol{x})$ of dimension 24 using the following definitions:

$$\mathbf{G}_1\left(\mathbf{F}^v, \mathbf{F}^e, \boldsymbol{d}\right) = \mathbf{F}^v - \mathbf{F}^v_n - \frac{\Delta t_n}{\eta_N} \left(\mathbf{F}^e\right)^\top \frac{\partial \Psi_{neq}}{\partial \mathbf{F}^e} \left(\mathbf{F}^e, \boldsymbol{d}\right) \mathbf{F}^v\,, \tag{19}$$

$$\mathbf{G}_2\left(\mathbf{F}^v, \mathbf{F}^e; \mathbf{F}\right) = \mathbf{F} - \mathbf{F}^e \mathbf{F}^v\,, \tag{20}$$

$$\boldsymbol{g}_3\left(\mathbf{F}^e, \hat{\boldsymbol{d}}, \boldsymbol{d}; \mathbf{F}\right) = \hat{\boldsymbol{d}} - \boldsymbol{d}_n - \Delta t_n \mathbf{W} \boldsymbol{d} + \frac{\Delta t_n}{\eta_D} \left(\mathbf{1} - \boldsymbol{d} \otimes \boldsymbol{d}\right) \frac{\partial \Psi}{\partial \boldsymbol{d}} \left(\mathbf{F}, \mathbf{F}^e, \boldsymbol{d}\right)\,, \tag{21}$$

$$\boldsymbol{g}_4\left(\hat{\boldsymbol{d}}, \boldsymbol{d}\right) = \hat{\boldsymbol{d}} - \boldsymbol{d} \left\|\hat{\boldsymbol{d}}\right\|\,, \tag{22}$$

where

$$\Delta t_n \mathbf{W} = \operatorname{skw}\left(\mathbf{1} - \mathbf{F}_n \mathbf{F}^{-1}\right)\,, \tag{23}$$

with the composite residual given as

$$\boldsymbol{g}\left(\boldsymbol{x}; \mathbf{F}\right) = \begin{bmatrix} \left(\mathbf{G}_1\left(\mathbf{F}^v, \mathbf{F}^e, \boldsymbol{d}\right)\right)_{vec} \\ \left(\mathbf{G}_2\left(\mathbf{F}^v, \mathbf{F}^e; \mathbf{F}\right)\right)_{vec} \\ \boldsymbol{g}_3\left(\mathbf{F}^e, \hat{\boldsymbol{d}}, \boldsymbol{d}; \mathbf{F}\right) \\ \boldsymbol{g}_4\left(\hat{\boldsymbol{d}}, \boldsymbol{d}\right) \end{bmatrix}\,, \tag{24}$$

where $\boldsymbol{x} = \left((\mathbf{F}^v)_{vec}^\top, (\mathbf{F}^e)_{vec}^\top, \hat{\boldsymbol{d}}^\top, \boldsymbol{d}^\top\right)^\top \in \mathbb{R}^{24}$ collects all the internal variables in a single vector; see Appendix A for how we map the components of tensors to vectors. The values of the internal variables $\boldsymbol{x}_{n+1} = \left((\mathbf{F}^v_{n+1})_{vec}^\top, (\mathbf{F}^e_{n+1})_{vec}^\top, \hat{\boldsymbol{d}}_{n+1}^\top, \boldsymbol{d}_{n+1}^\top\right)^\top$ corresponding to $\mathbf{F}_{n+1}$ are the solution of

$$\boldsymbol{g}\left(\boldsymbol{x}; \mathbf{F}_{n+1}\right) = \mathbf{0}\,. \tag{25}$$

Remark 4. Note that even though we can solve fewer equations if we use (20) to substitute $\mathbf{F}^e = \mathbf{F}\left(\mathbf{F}^v\right)^{-1}$ into (19) and (21), we may run into trouble if one of the iterates for $\mathbf{F}^v$ is singular. The augmented set of equations avoids this problem. A similar point can also be made with respect to solving (22) for $\boldsymbol{d}$ and substituting into the other expressions; the utility of not doing so comes in terms of substantial simplifications in computing derivatives and robustness with respect to non-physical corner cases that can appear during nonlinear iterations.

3.1.2 Local Newton-Raphson Tangent

To solve (25) for $\boldsymbol{x}$, the derivative of $\boldsymbol{g}$ with respect to $\boldsymbol{x}$ is required for Newton-Raphson iterations. Accordingly we require derivatives of the sub-residuals of $\boldsymbol{g}$ with respect to the elements of $\boldsymbol{x}$. We collect these in a 24×24 matrix:

$$\frac{\partial \boldsymbol{g}}{\partial \boldsymbol{x}}\left(\boldsymbol{x}; \mathbf{F}_{n+1}\right) = \begin{bmatrix} (\partial \mathbf{G}_1/\partial \mathbf{F}^v)_{9\times 9} & (\partial \mathbf{G}_1 \partial \mathbf{F}^e)_{9\times 9} & \mathbf{0}_{9\times 3} & (\partial \mathbf{G}_1/\partial \boldsymbol{d})_{9\times 3} \\ (\partial \mathbf{G}_2/\partial \mathbf{F}^v)_{9\times 9} & (\partial \mathbf{G}_2/\partial \mathbf{F}^e)_{9\times 9} & \mathbf{0}_{9\times 3} & \mathbf{0}_{9\times 3} \\ \mathbf{0}_{3\times 9} & (\partial \boldsymbol{g}_3/\partial \mathbf{F}^e)_{3\times 9} & \partial \boldsymbol{g}_3/\partial \hat{\boldsymbol{d}} & \partial \boldsymbol{g}_3/\partial \boldsymbol{d} \\ \mathbf{0}_{3\times 9} & \mathbf{0}_{3\times 9} & \partial \boldsymbol{g}_4/\partial \hat{\boldsymbol{d}} & \partial \boldsymbol{g}_4/\partial \boldsymbol{d} \end{bmatrix}. \tag{26}$$

The subscripts on the entries identify the sizes of the blocks under particular tensor-vector mappings. The computation of the blocks is straight-forward but intricate and the detailed expressions are listed in Appendix B.

Remark 5. Applying a Newton-Raphson method, we can solve (25) for the internal variables $\boldsymbol{x}_{n+1}$ with local quadratic convergence. In our implementation, we augment the standard Newton procedure with a simple line search that recursively bisects the search step should the local residual grow more than 10% of the initial value. While this is not a guarantee of local convergence, it provides substantial robustness to the local iterator.

3.2 Element Residual

Since the director is treated as an internal variable, we only have three displacement degrees of freedom at each node in a three-dimensional problem. Employing standard finite element

procedures, see e.g. Zienkiewicz et al. (2013, 2014), we express the displacement field for an element e which occupies $\Omega_0^e \subset \mathcal{B}$ with NEN nodes as

$$\boldsymbol{u}^e = \sum_{i=1}^{NEN} N_i \boldsymbol{u}_i^e = \begin{bmatrix} N_1 \mathbf{1}_{3\times 3} & N_2 \mathbf{1}_{3\times 3} & \dots & N_{NEN} \mathbf{1}_{3\times 3} \end{bmatrix} \begin{bmatrix} \boldsymbol{u}_1^e \\ \boldsymbol{u}_2^e \\ \dots \\ \boldsymbol{u}_{NEN}^e \end{bmatrix} = \mathbf{N} \hat{\boldsymbol{u}}^e \,, \tag{27}$$

where N_i is the shape function corresponding to node i, $\boldsymbol{u}_i^e$ is the displacement of node i, and $\mathbf{1}_{3\times 3}$ is the 3×3 identity matrix. Applying the same approximation to the test function in (2), we get

$$\delta \boldsymbol{\varphi} = \mathbf{N} \delta \hat{\boldsymbol{\varphi}} \,. \tag{28}$$

Adopting the tensor-to-vector mapping from (46), the gradient of (28) is

$$(\operatorname{Grad} \delta \boldsymbol{\varphi})_{vec} = \begin{bmatrix} \delta \boldsymbol{\varphi}_{,1} \\ \delta \boldsymbol{\varphi}_{,2} \\ \delta \boldsymbol{\varphi}_{,3} \end{bmatrix} = \begin{bmatrix} \mathbf{N}_{,1} \delta \hat{\boldsymbol{\varphi}} \\ \mathbf{N}_{,2} \delta \hat{\boldsymbol{\varphi}} \\ \mathbf{N}_{,3} \delta \hat{\boldsymbol{\varphi}} \end{bmatrix} = \mathbf{B} \delta \hat{\boldsymbol{\varphi}} \,, \tag{29}$$

where the sparse $9 \times 3NEN$ gradient operator

$$\mathbf{B} = \begin{bmatrix} \mathbf{B}_1 & \mathbf{B}_2 & \dots & \mathbf{B}_{NEN} \end{bmatrix} \,, \tag{30}$$

within which

$$\mathbf{B}_i = \begin{bmatrix} N_{i,1} \mathbf{1}_{3\times 3} \\ N_{i,2} \mathbf{1}_{3\times 3} \\ N_{i,3} \mathbf{1}_{3\times 3} \end{bmatrix} \,. \tag{31}$$

Therefore, the integrand at time t_{n+1} in (2) may be computed as

$$\mathbf{P}_{n+1} : \operatorname{Grad} \delta \boldsymbol{\varphi} = (\mathbf{P}_{n+1})_{vec} \cdot (\operatorname{Grad} \delta \boldsymbol{\varphi})_{vec} = \delta \hat{\boldsymbol{\varphi}}^\top \mathbf{B}^\top (\mathbf{P}_{n+1})_{vec} \,. \tag{32}$$

Accordingly, the time t_{n+1} element residual is computed as:

$$\boldsymbol{r}_{n+1}^e = \int_{\Omega_0^e} \mathbf{B}^\top (\mathbf{P}_{n+1})_{vec} \, dV \,. \tag{33}$$

3.3 Element Tangent

To compute the element tangent, we must consider the directional derivative of (32) with respect to the nodal displacements in the direction of an increment $\Delta \boldsymbol{u}$:

$$\begin{aligned} \Delta \mathbf{P}_{n+1} : \operatorname{Grad} \delta \boldsymbol{\varphi} &= \operatorname{Grad} \delta \boldsymbol{\varphi} : \left(\frac{d \mathbf{P}_{n+1}}{d \mathbf{F}_{n+1}} : \operatorname{Grad} \Delta \boldsymbol{u} \right) \\ &= (\operatorname{Grad} \delta \boldsymbol{\varphi})_{vec} \cdot \left(\frac{d \mathbf{P}_{n+1}}{d \mathbf{F}_{n+1}} \right)_{9\times 9} (\operatorname{Grad} \Delta \boldsymbol{u})_{vec} \\ &= \delta \hat{\boldsymbol{\varphi}}^\top \mathbf{B}^\top \left(\frac{d \mathbf{P}_{n+1}}{d \mathbf{F}_{n+1}} \right)_{9\times 9} \mathbf{B} \, \Delta \hat{\boldsymbol{u}} \,. \end{aligned} \tag{34}$$

The *total derivative* of the first Piola-Kirchhoff stress with respect to the current deformation gradient $\mathbf{F}_{n+1}$ is composed of three terms, the last two of which account for the integration of the internal variables:

$$\left(\frac{d\mathbf{P}_{n+1}}{d\mathbf{F}_{n+1}}\right)_{iAjB} = \left(\frac{\partial\mathbf{P}_{n+1}}{\partial\mathbf{F}_{n+1}}\right)_{iAjB} + \left(\frac{\partial\mathbf{P}_{n+1}}{\partial\mathbf{F}^e_{n+1}}\right)_{iAp\alpha}\left(\frac{\partial\mathbf{F}^e_{n+1}}{\partial\mathbf{F}_{n+1}}\right)_{p\alpha jB} + \left(\frac{\partial\mathbf{P}_{n+1}}{\partial\boldsymbol{d}_{n+1}}\right)_{iAp}\left(\frac{\partial\boldsymbol{d}_{n+1}}{\partial\mathbf{F}_{n+1}}\right)_{pjB} . \tag{35}$$

The first term, the partial derivative of (15) with respect to $\mathbf{F}_{n+1}$, is

$$\left(\frac{\partial\mathbf{P}_{n+1}}{\partial\mathbf{F}_{n+1}}\right)_{iAjB} = \mathrm{sym}_{ik}\left(\mathcal{A}_{iDjB}\left(\mathbf{F}_{n+1}\right)_{kD} + \mathrm{Q}_{iB}\delta_{kj}\right)\left(\mathbf{F}^{-1}_{n+1}\right)_{Ak} - \left(\mathbf{P}_{n+1}\right)_{iB}\left(\mathbf{F}^{-1}_{n+1}\right)_{Aj} , \tag{36}$$

where we have made use of the symbols $\mathbf{Q}$ and $\mathcal{A}$ defined in (51) and (52) in Appendix B, and the operator sym_{ik} implies symmetrization with respect to the ik indices. Similarly, the partial derivative of (15) with respect to $\mathbf{F}^e_{n+1}$ is

$$\left(\frac{\partial\mathbf{P}_{n+1}}{\partial\mathbf{F}^e_{n+1}}\right)_{iAp\alpha} = \mathrm{sym}_{ik}\left(\mathcal{A}^e_{i\beta p\alpha}\left(\mathbf{F}^e_{n+1}\right)_{k\beta} + \mathrm{Q}^e_{i\alpha}\delta_{kp}\right)\left(\mathbf{F}^{-1}_{n+1}\right)_{Ak} . \tag{37}$$

The symbols $\mathbf{Q}^e$ and $\mathcal{A}^e$ are defined in (51) and (52) in Appendix B. And finally, the partial derivative of (15) with respect to $\boldsymbol{d}_{n+1}$ is

$$\left(\frac{\partial\mathbf{P}_{n+1}}{\partial\boldsymbol{d}_{n+1}}\right)_{iAj} = \mathrm{sym}_{ik}\left(\mathcal{M}_{iDj}\left(\mathbf{F}_{n+1}\right)_{kD} + \mathcal{M}^e_{i\alpha j}\left(\mathbf{F}^e_{n+1}\right)_{k\alpha}\right)\left(\mathbf{F}^{-1}_{n+1}\right)_{Ak} . \tag{38}$$

The symbols $\mathcal{M}$ and $\mathcal{M}^e$ are defined in (53) in Appendix B.

Lastly, to complete the computation of the total derivative of the stress with respect to the current deformation gradient $\mathbf{F}_{n+1}$, the derivatives of the internal variables $\boldsymbol{d}_{n+1}$ and $\mathbf{F}^e_{n+1}$ with respect to $\mathbf{F}_{n+1}$ are needed. This is computed by taking the total derivative of (25) with respect to $\mathbf{F}_{n+1}$ and applying the chain rule:

$$\left(\frac{\partial\boldsymbol{x}_{n+1}}{\partial\mathbf{F}_{n+1}}\right)_{24\times 9} = -\left(\frac{\partial\boldsymbol{g}}{\partial\boldsymbol{x}}\left(\boldsymbol{x}_{n+1};\mathbf{F}_{n+1}\right)\right)^{-1}\left(\frac{\partial\boldsymbol{g}}{\partial\mathbf{F}}\left(\boldsymbol{x}_{n+1};\mathbf{F}_{n+1}\right)\right)_{24\times 9} . \tag{39}$$

From (39), one can extract the necessary terms to compute (35). Also note that the required derivatives are known from the evaluation of the stress and thus no additional computations are required.

Finally, the element tangent for non-linear iterations is

$$\mathbf{K}^e_{n+1} = \int_{\Omega^e_0}\mathbf{B}^\top\left(\frac{d\mathbf{P}_{n+1}}{d\mathbf{F}_{n+1}}\right)_{9\times 9}\mathbf{B}\,dV . \tag{40}$$

Remark 6. As is not always seen in the LCE literature, the necessary tangent operator is computed with respect to the actual integration algorithm used to update the internal variables and which ensures global (asymptotic) quadratic convergence.

Remark 7. Formulating (33) and (40) in first Piola-Kirchhoff format reduces the necessary computations. If one uses the more traditional forms that operate on the Kirchhoff stress and its variation, one is faced with numerous extra computational steps. In particular, to compute the Kirchhoff stress and its variation, we *must* compute the first Piola-Kirchhoff stress and its variation first. Then these tensors must be "pushed forward" to the current configuration. This extra work provides no downstream computational advantages – it is completely unnecessary. Appendix C provides further details.

4 Numerical Examples

The results discussed below were obtained using an implementation of the theory just discussed in the general purpose code FEAP by Taylor and Govindjee (2020). All the simulations's time steps converge quadratically using Newton's method with a line search. Visualizations were generated within Paraview (Ahrens et al., 2005). Even though the material is rather incompressible, we can utilize standard displacement based elements due to the lack of material confinement in our examples. In general, however, the element formulation should be adapted to employ F-bar or similar methods; see e.g. Zienkiewicz et al. (2014) and references therein.

Remark 8. We are not guaranteed the existence of solutions prior to running the simulations. In particular in the zero-viscosity limit, the neo-classical model upon which we base our computations generates a variational minimization problem whose underlying energy density is not quasiconvex – a necessary condition for the existence of minimizers (Dacorogna, 2008; DeSimone and Dolzmann, 2002). Nonetheless, at finite viscosities we observe solutions that are stable and show proper mesh convergence.

4.1 Extension and unloading of an LCE specimen

For our first example, we simulate the classic LCE tension experiment. This example involves a material displaying soft elasticity and highlights unique issues that arise in boundary value problems as compared to material point calculations.

4.1.1 Material

The material model for our tension test will be a neo-Gent model (9) for both the equilibrium and non-equilibrium energies, and the material parameters are obtained from a parameter fitting done by Wang et al. (2022) to the data of Linares et al. (2020). As reported by Wang et al. (2022), the equilibrium shear modulus $\mu_{eq} = 0.25$ MPa, the non-equilibrium shear modulus $\mu_{neq} = 1.25$ MPa, the Gent stiffening parameter $J_m = 5.7$ (for both energies), and

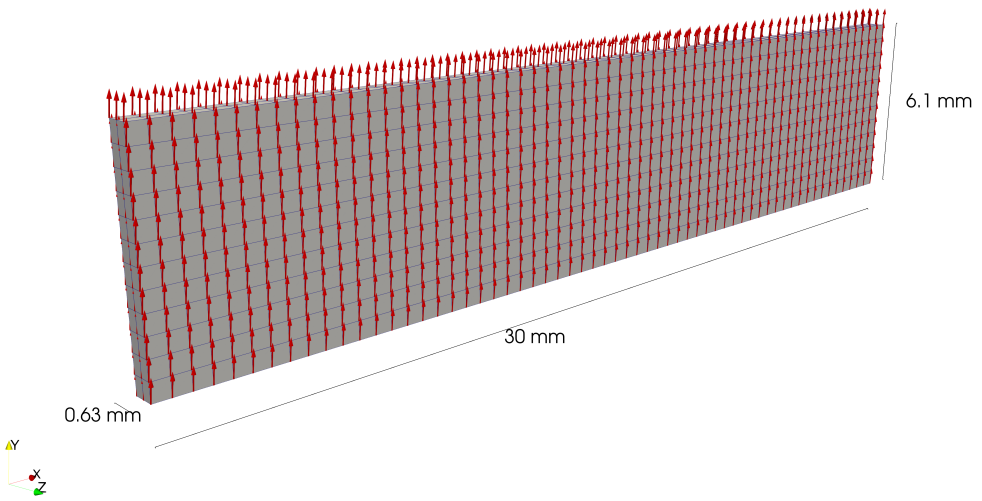

Figure 2: Finite element mesh of the LCE specimen with the director shown as red arrows.

the anisotropy/step-length ratio $r = 5.89$. Furthermore, the initial director viscosity was found to be $\eta_D = 40$ MPa $\cdot$ s and the network viscosity was found to be $\eta_N = 800$ MPa $\cdot$ s. The director viscosity in Wang et al. (2022) was nonlinear and assumed a value of 16 MPa $\cdot$ s during the rotational phase of the deformation. In our FEA simulations we will simply use a constant value of $\eta_D = 16$ MPa $\cdot$ s. Additionally, the Lamé parameters used are $\Lambda_{eq} = 500$ MPa and $\Lambda_{neq} = 0$ MPa.

4.1.2 Specimen geometry and boundary conditions

We assume the test specimen of Linares et al. (2020) of length 30 mm, width 6.1 mm, and thickness 0.63 mm. The loading is imposed displacement in the longitudinal direction with clamped conditions; i.e. on one end $\boldsymbol{u} = \boldsymbol{0}$ (fixed) and on the other end $u_y = u_z = 0$ with an imposed u_x (see Fig. 2 for the axes orientation with respect to the specimen). The motion is imposed at a constant displacement rate $\dot{u}_x = 3$ mm/s until $u_x = 100$ mm, which is then followed by unloading at the same displacement rate. The constant rate unloading continues until the distance between the clamps reaches 30 mm – the initial sample length. The initial director field in the classical soft-elasticity experiment is assumed to be uniform $\boldsymbol{d}_0(\boldsymbol{X}) = \boldsymbol{e}_y$ as shown in Fig. 2. The stretch in the FEA simulation is computed using a 18 mm gauge in the center of the specimen.

4.1.3 Approximate stress point response

If one ignores end-effects the system is reasonably idealized as being in a homogeneous state of uniaxial tension. As such, the stress response of the material in the boundary value problem

can be computed as a material point computation. In Wang et al. (2022) this was done and shown to produce physically realistic behavior in loading and unloading in comparison to experimental data from Linares et al. (2020). A nuance of the computation however was that the initial director value was perturbed using a small rotation $\boldsymbol{Q}_z(\omega)$ about the z-axis. Without the perturbation, the director remains in an unstable equilibrium position as the right-hand side of (6) will be zero. This produces unphysical results. The perturbation avoids this problem in the material point computation. Note that the perturbation can be either clockwise or counter-clockwise and not affect the stress response. As is well established in the neo-classical elastic case (see e.g. Warner and Terentjev, 2003), there are two stable equilibrium states for the director in the material point problem – a clockwise or counter-clockwise rotation of the same magnitude about the z-axis. Both produce the same stress response and one or a mixture of the two needs to be selected.

4.1.4 Boundary value problem with uniformly perturbed director field

When looking at boundary value problems, the same issue of unstable equilibria exists as with material point computations. This is not too dissimilar from the case of compression of a slender bar or necking of a rod. A perturbation is required to bias the system towards the correct equilibrium configuration. As a first choice we consider a homogeneous perturbation of all the directors by a rotation $\boldsymbol{Q}_z(\omega)$, where $\omega = -1.0°$.

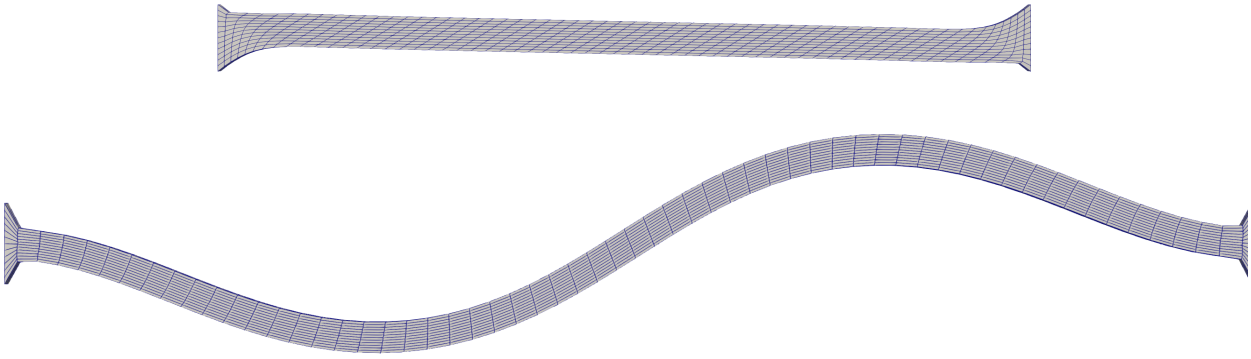

Figure 3: (top) Homogeneously perturbed director field specimen at an average stretch $\lambda_x = 1.46$ during loading and (bottom) at $\lambda_x = 2.17$ during the unloading process from a maximum average stretch of $\lambda_x = 4.6$.

As the sample is stretched, the director rotates to align with the loading direction, during which the stress reaches a plateau. After director alignment, the network chains are stretched and an increase in stress is observed. Upon unloading the rotated directors remain rotated and the sample retracts viscoelastically. The unloading protocol continues until the distance between the ends reaches the initial length. There are three principal observations:

1. The force-displacement/stress-strain response largely matches that seen in a material point computation. See Fig. 4 where the gold curve is the constant director viscosity

FEA computation and the red curve is the nonlinear viscosity material point computation from Wang et al. (2022); the experimental data is shown in blue. The primary difference between the FEA and the material point result is that the FEA boundary value problem avoids the sharp over-shoot peak seen in the material point computation. This is likely due to the inhomogeneous region near the clamps promoting director rotation.

2. The deformation pattern upon extension demonstrates significant shear. In particular, Fig. 3 (top) shows the specimen at an extension of 44 mm (average stretch $\lambda_x = 1.47$) early in the extension process. One observes a strong shearing throughout (due to director rotation) and a strong anti-symmetric pattern near the ends. This macroscopic shear behavior can occur experimentally, depending on strain rate and the degree of mesogen alignment Linares et al. (2020).

3. Upon unloading, Fig. 3 (bottom) shows that the specimen has buckled nonphysically about the strong-axis, something not seen experimentally Linares et al. (2020).

One can largely conclude that the use of a homogeneously perturbed director field is inappropriate in the solution of boundary value problems using LCE models of the class presented even though that is effective in a material point computation.

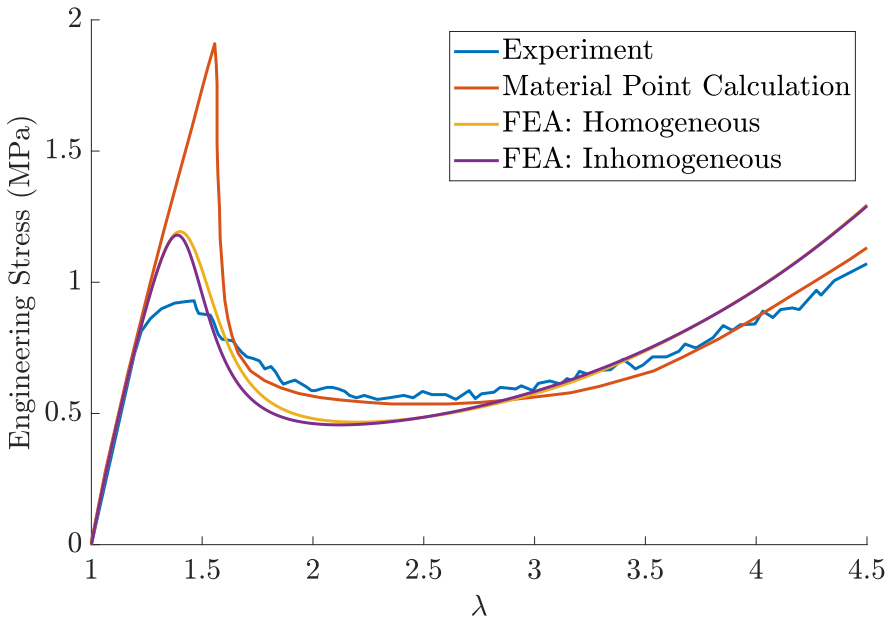

Figure 4: Comparison between the experimental, nonlinear viscosity material point calculation from Wang et al. (2022), and the constant viscosity FEA computations with homogeneous and inhomogeneous initial director fields.

4.1.5 Boundary value problem with an inhomogeneously perturbed director field

We note that in the fully elastic case, there are two stable equilibiria during extension (Warner and Terentjev, 2003). If one assumes a maximum entropy response of the system, then one should expect to see directors rotating clockwise and counter-clockwise with equal probability. In fact this has been observed in experiments by Kundler and Finkelmann (1995) via the presence of alternating strips of material displaying plus/minus shears in the xy-plane. To test this, consider an inhomogeneous initial director field $\boldsymbol{d}_0(\boldsymbol{X})$ that is selected such that 50% of the directors are perturbed by $\boldsymbol{Q}_z(\omega)$ and 50% are perturbed by $\boldsymbol{Q}_z(-\omega)$, where $\omega = 1°$. The precise spatial pattern we use is one where the perturbation alternates as one moves from one row of elements to the next in the y-direction; put another way, the director perturbation changes algebraic sign every 0.5 mm in the y-direction and is uniform in the x- and z-directions.

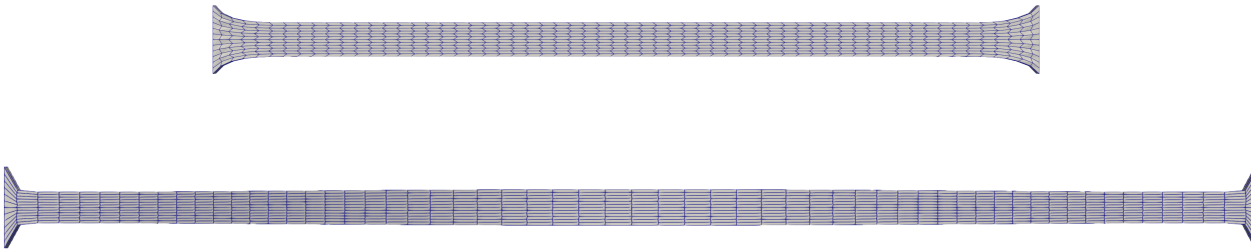

Figure 5: (top) Inhomogeneously perturbed director field specimen at an average stretch $\lambda_x = 1.46$ during loading and (bottom) at $\lambda_x = 2.17$ during the unloading process from a maximum average stretch of $\lambda_x = 4.6$.

The result of the use of this inhomogeneous initial director field yields the results seen in Fig. 5; cf. Fig. 3 where a homogeneous initial director field was used. The following observations can be made:

1. The force-displacement/stress-strain response during loading matches that seen in the homogeneously perturbed director case; see the purple line in Fig. 4. For the inhomogeneous and homogenous case, the stress-strain curves agree well with experiments, and the sharp over-shoot in the stress response of the material point calculation is avoided. The stress response of the homogeneous and inhomogeneous case differs slightly during mesogen rotation, where the stress decays from the peak to a semi-soft plateau. The semi-soft plateau is lower than for the material point calculation, which used a nonlinear viscoelastic model to fit the plateau stress to experiments. As expected, the initial and large deformation viscoelastic network behavior are identical.

2. The extensional behavior seen in Fig. 5 (top) does not show pronounced macroscopic shear. A close examination of the deformed mesh shows that the alternate rows of

elements are shearing plus/minus and thus on average give zero net shear – a point that is consistent with the standard explanation of soft-elasticity Warner and Terentjev (2003). This deformation behavior is also observed in experiments, depending on loading rate and the degree of mesogen alignment Linares et al. (2020).

3. At the average stretch $\lambda_x = 2.17$ during the unloading, the specimen does not display nonphysical buckling as was seen in the homogeneously perturbed case.

4. If the specimen is unloaded all the way back to an average stretch $\lambda_x = 1$, then it does buckle (see Fig. 6), but now in the physically correct way about the weak axis – something that is compatible with experimental observations.

5. The observed behavior of the directors in this example where they rotate alternately in clockwise and counter-clockwise directions in reminiscent of the formation of fine-scale microstructure. A natural question that arises in such situations is whether the model is well posed with respect to refinements in microstructure. Shown in Fig. 7 is the load displacement response during the loading phase up to an average stretch of $\lambda_x = 3.33$ at 4 mesh refinement levels. Note that as the mesh is refined, the initial director field is also refined such that the oscillations in the perturbation become finer and finer. Thus the initial director field is converging in measure to a distribution defined by two equally weighted Dirac masses in this process. While we can not mathematically prove convergence, we do claim that this computation shows stable convergence behavior based on Fig. 7.

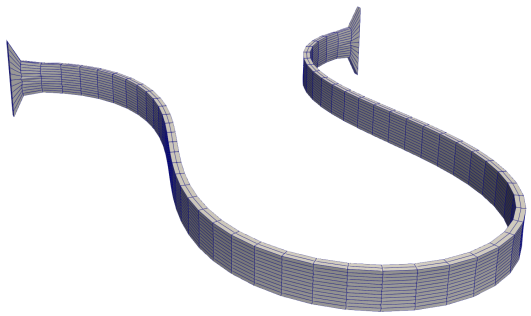

Figure 6: Weak axis bucking of the inhomogeneously perturbed specimen. End separation is 30 mm.

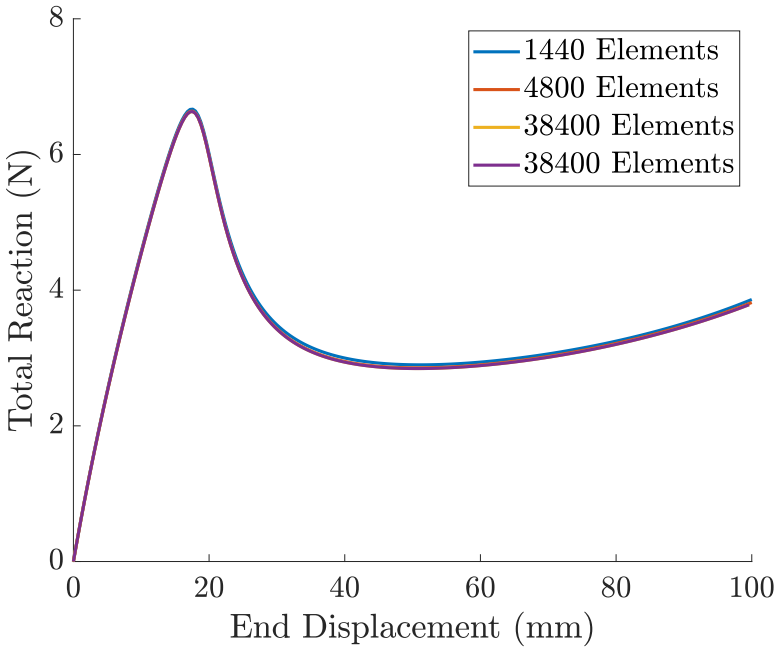

Figure 7: Convergence of load-displacement response as the mesh size decreases while refining the initial director field.

4.2 Compression of a Cylinder

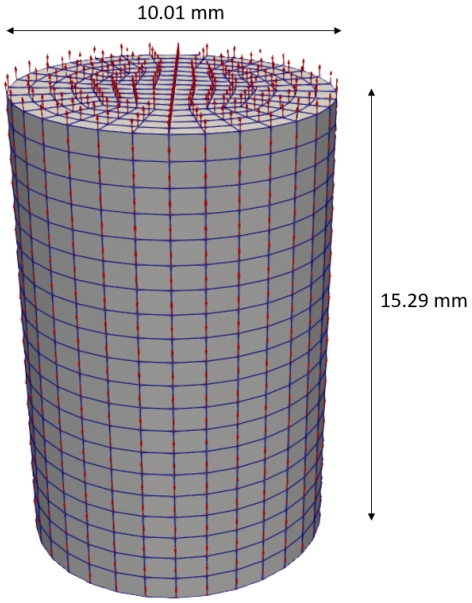

Figure 8: Finite element mesh of the LCE cylinder with the initial directors shown as red arrows.

The tension of LCE materials is well studied experimentally and theoretically. On the other hand, less is known about the compression of LCEs, and thus we consider the uniaxial compression of an LCE cylinder. Below we first describe a qualitative compression test, followed by a quantitative experiment.

4.2.1 Methods and materials

Monodomain cylinders were provided by Impressio (Denver, CO, USA). Pillars were designed to match the chemical, mechanical, and morphological behavior of previous studies (Yakacki et al., 2015; Saed et al., 2017) These studies utilized a two-stage thiol-acrylate Michael addition reaction followed by mechanical alignment and a photopolymerization reaction to program main-chain monodomain samples. In general, samples are made from 2,2′-(Ethylenedioxy)diethanethiol (EDDET), Pentaerythritol tetrakis(3-mercaptopropionate) (PETMP), and 1,4-Bis-[4-(3-acryloyloxypropyloxy) benzoyloxy]-2-methylbenzene (RM257). Specific catalysts, initiators, and processing conditions are, however, proprietary to Impressio. The director is nominally homogeneously aligned in the z-direction and the anisotropy/step-length ratio $r = 5.5$, which corresponds to a scalar order parameter $Q = 0.6$.

The quantitative experiment conducted was a quasi-static uniaxial compression test under displacement control in an MTS Insight 5 equipped with a 500 N load cell (Eden Prairie, MN, USA). The monodomain LCE cylinder measured $d = 10.01$ mm in diameter and $h = 15.29$ mm in height as depicted in Fig. 8, which also shows the finite element mesh used in our computations. The LCE cylinders were placed on the bottom compression platen lined with sandpaper to increase friction. The upper compression platen was lowered manually onto the specimen until the force reached 0.06 N to ensure full contact with the specimen. The 0.06 N force threshold was determined from the maximum fluctuations of the 500 N load cell reading at zero load. The load cell was then zeroed to start the compression test. The rate of compression was $\dot{u}_z = 7.7 \times 10^{-3}$ mm/s and the specimen was compressed to a stretch of $\lambda_z = 0.58$. In all the computations reported below, the boundary conditions on the top and bottom were stick, so $u_r = u_\theta = 0$ with an imposed value of u_z, where z is the axial coordinate of the cylinder.

4.2.2 Qualitative experimental behavior

Figure 9 shows two compression experiments on two different specimen. On the left, the we see a specimen after being compressed and then unloaded. On the right we see a second specimen in the loaded state with $\lambda_z = 0.5$. The first experiment shows significant preferential bulging and shearing in one direction in the cylinder. In contrast, the second experiment does not show any significant shearing as the sample is compressed, but instead shows relatively uniform rippling and wrinkling in the specimen. Both experiments show an anisotropic change in the circular cross section to an elliptical cross section. This suggests director rotation into the plane normal to the cylinder axis, with the rotation occurring in the plane defined by the axis of the cylinder and the major axis of the ellipse.

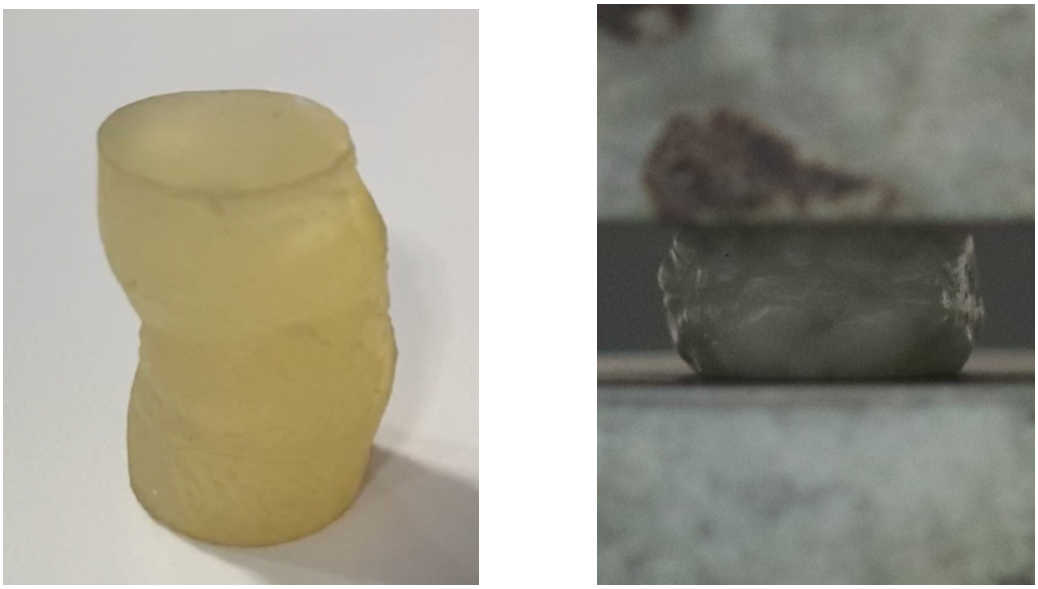

Figure 9: Snapshot of the deformed LCE cylinders in two compression experiments. The (left) experiment shows bulging to one side after loading and unloading. The (right) experiment shows rippled bulging in all directions at a compressed stretch of $\lambda_z = 0.5$.

4.2.3 Choice of initial director field and qualitative response

We explored several choices for the initial director field to qualitatively understand the experimental observations. In particular, we were interested to understand if the initial director field was responsible for the different behaviors seen in compression. Figure 10 shows the result of this exploration. On the left one sees a compression simulation which utilizes a homogeneous initial director field that is perturbed by a rotation $\boldsymbol{Q}_x(\omega)$, where $\omega = -1°$; i.e. the initial director field, $\boldsymbol{d}_0(\boldsymbol{X}) = \boldsymbol{Q}_x(\omega)\boldsymbol{e}_z$, is a one-degree rotation about a fixed axis orthogonal to the lateral surface of the cylinder. On the right one sees a compression simulation which utilizes an inhomogeneous initial director field. Here the perturbation is formed from an alternating pattern (in the z-direction) of plus/minus rotations about the fixed x-axis – i.e. a 50-50 mixture of clockwise and counter-clockwise $1°$ perturbations as one moves up the cylinder. We make the following observations:

1. The qualitative deformation patterns are qualitatively well reproduced via the selection of different initial director fields.

2. Both initial director fields represent nominally z-oriented homogeneous initial director fields. However the response of LCE materials, depending on the character of the load, can be quite sensitive to the details of the initial director field. This presents a challenge to designing mechanical systems utilizing these materials.

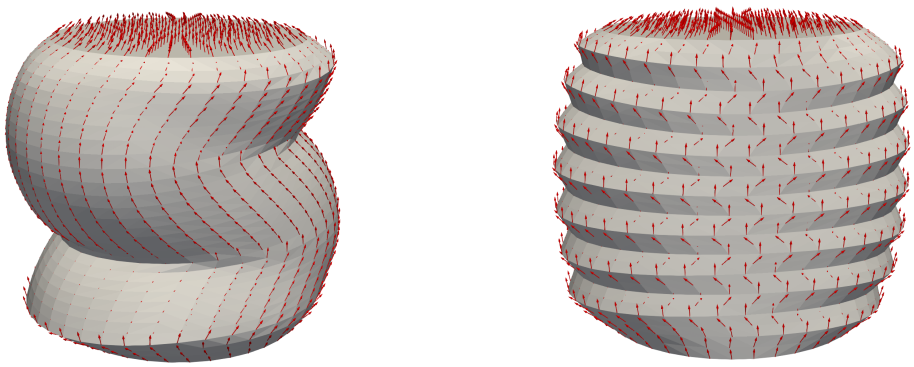

Figure 10: Snapshot of the deformed LCE cylinders in the two simulations as they are compressed. The first simulation (left) has a homogeneous initial director field while the second (right) has an inhomogeneous initial director field.

4.2.4 Quantitative comparison to experiments

We also make an assessment of the quantitative quality of our finite element simulations. In particular, we examine the degree to which the load-deflection response can be replicated for an experiment where an inhomogeneous initial director field was the most appropriate. The load-deflection data for this particular cylinder is shown in Fig. 11 by the blue curve. As previously mentioned, the rate of compression was $\dot{u}_z = 7.7 \times 10^{-3}$ mm/s and the specimen was compressed to a stretch of $\lambda_z = 0.58$.

In Wang et al. (2022), it was shown that network viscoelasticity plays a role mainly after the soft region in tension, when the largest stretch exceeds $\sqrt{r}$. For compression, the soft region theoretically extends down to a stretch of $\lambda = 1/\sqrt{r}$ which corresponds to a displacement of around 8.6 mm. Conjecturing that the viscoelastic behavior is the same in compression as in tension, we choose to ignore the viscoelasticity in our computations as the maximum displacement in the experiments was 6.36 mm; director viscosity, however, is not ignored. Note we did test this conjecture by also running a handful of computations with viscoelasticity and seeing that viscoelasticity did not alter the load-deflection behavior in the range of the experiments. We also note that at these levels of deformation, we are well away from the chain locking-stretch for the material. For this reason we choose to use a neo-classical energy function for the equilibrium free energy for the material.

Shown in Fig. 11 are a series of load-displacement curves at varying mesh densities. As in the tension case the initial inhomogeneous director field is also refined as the mesh is refined. For the computations the shear modulus $\mu_{eq} = 0.2$ MPa was chosen so that the initial slope of the loading curves matched the experimental curve. From the results, we verify that the computations do converge. The Lamé parameter was $\Lambda_{eq} = 100$ MPa.

We also find in this computation, that the agreement with the data shown requires the use

of a nonlinear director viscosity. We find that a constant director viscosity results in large overshooting of the data in the early part of the deformation, if one requires matching the later part of the deformation. A similar situation was reported in Wang et al. (2022) where a nonlinear viscosity was found necessary in the matching to experimental tensile data. The nonlinear viscosity which we found effective here is

$$\eta_D = \frac{9.0}{\pi}\arctan\left[300.0\left(\|\tilde{\mathbf{F}}\| - 1.74\right)\right] + 5.5\ (\text{MPa}\cdot\text{s})\,, \tag{41}$$

where $\|\tilde{\mathbf{F}}\|$ is the norm of the isochoric part of the deformation gradient. In particular, the viscosity rises upon increasing compression and then saturates. The increasing viscosity function dramatically reduces the stress overshoot, but does not remove the softening behavior entirely. This phenomenological function is likely not generalizable to other deformation modes but does suggest the required behavior in compression.

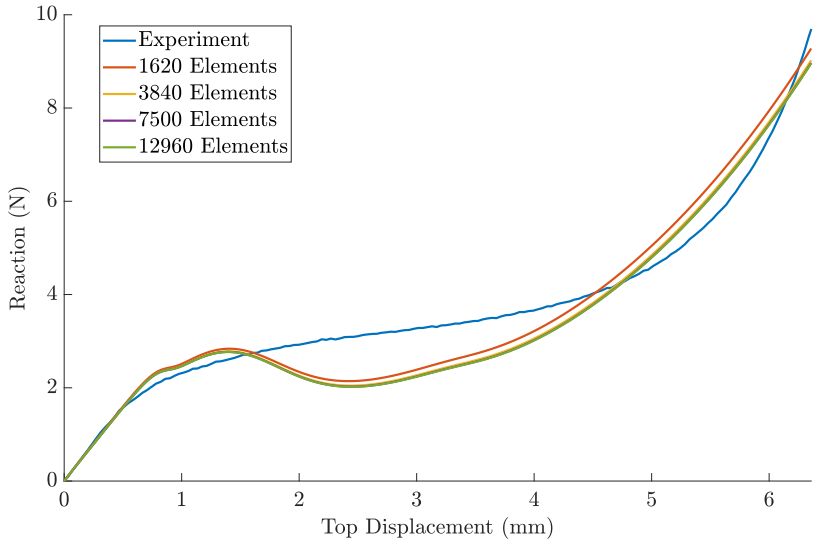

Figure 11: Experimental and computed force-deflection response of a cylinder with an inhomogeneous initial director field at different levels of mesh refinement and a nonlinear director viscosity.

4.3 Inflation of an LCE Balloon

As a last example we consider the interesting experiment of He et al. (2020) on the inflation of an LCE balloon. These authors consider a monodomain thick-walled balloon with inner radius 4 mm, outer radius 5 mm, and length of 120 mm. The initial director is aligned with the tube axis. The balloon has an acrylic rod glued into one end, while an acrylic tube is glued into the other end. Inflation pressure is applied to the inside of the tube with a custom-built controller. During inflation, the balloon first responds in a stiff manner, then suddenly *contracts* axially while expanding radially, then the balloon grows in size radially and axially, followed by a pressure instability (limit load), jumping to a new stable equilibrium at a much greater size.

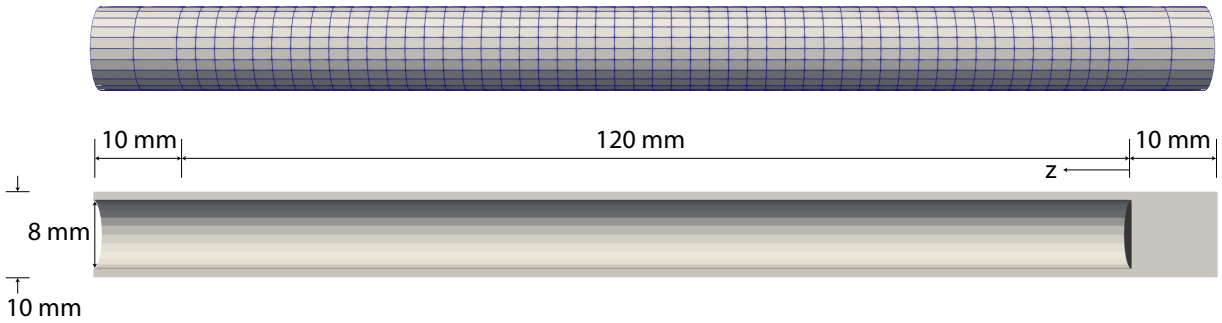

Figure 12: Finite element mesh and cross-section with dimensions.

The balloon material's properties are partially characterized in the paper, giving an initial shear modulus of 0.8 MPa and an anisotropy/step-length ratio $r = 1/0.19 = 5.26$; the characterization is performed via uniaxial extension at a strain rate of 5×10^{-4} sec^{-1}. The balloon's material is stated to have a weak rate dependence but the director viscosity and network viscosity were not explicitly reported. Thus here we do not attempt a precise fit to the experiments and in fact we use a relatively coarse mesh, leading to a somewhat stiff response.

To simulate the experiment, we construct a mesh for the central section of the tube of length 120 mm using 50 elements axially, 4 elements through the thickness, and 24 elements along the hoop direction; see Fig. 12. The tube is extended 10 mm at both ends. At one end the tube is filled within the extension with a material with moduli that are 1000 times that of the main tube, effectively rendering the material rigid, thereby modeling the acrylic rod. Within the other extension, the nodes on the inner radius are fixed from moving in all three coordinate directions to mimic the glued-in acrylic tube. The inner surfaces of the central section and the bottom plug are subjected to follower-type pressure loads.

For the simulation we use an equilibrium shear modulus of $\mu_{eq} = 0.8$ MPa (as measured), and an anisotropy/step-length ratio $r = 5.26$ (as measured), and bulk modulus $\Lambda_{eq} = 200$ MPa. The non-equilibrium moduli are taken as $\mu_{neq} = 0.4$ MPa and $\Lambda_{neq} = 0$ MPa for illustrative purposes. For our numerical experiment, we consider the neo-Gent model for the equilibrium

response (9) and a neo-classical model (8) for the non-equilibrium response. Our network viscosity is taken as $\eta_N = 0.1$ MPa $\cdot$ s, our baseline director viscosity is taken as $\eta_D = 0.01$ MPa $\cdot$ s, our Gent parameter is taken as $J_m = 30$, and our pressure loading is linear in time, $p(t) = \dot{p}\, t$, where $\dot{p} = 4.0$ kPa $\cdot$ sec^{-1}. Again, all these parameters are for illustration since they were not reported in the original paper. Further we assume a mass density $\rho = 1.1 \times 10^{-9}$ Mg/mm^3.

Numerous experimental variations, including those lifting weights, are shown in He et al. (2020) along with the response of a simple model that assumes the balloon to be thin-walled, infinitely long, and characterized by the neo-classical model in the form presented by Conti et al. (2002). Here we focus on the experiment where no weights are hung from the balloon. Our goals are (1) to demonstrate our numerical implementation on a complex initial boundary value problem and (2) to further elucidate the behavior seen in the experiment.

As in He et al. (2020), we focus on the pressure-stretch response for an average axial stretch and a select hoop stretch. In particular, two points $\mathbf{X}^{(1)}$ and $\mathbf{X}^{(2)}$ located on the outer surface at $z = 90.2$ mm and $z = 19.8$ mm, respectively, are used to define an average axial stretch for the tube $\bar{\lambda}_z = (u_z(\mathbf{X}^{(1)}) - u_z(\mathbf{X}^{(2)}))/(z^{(1)} - z^{(2)})$. The location $z = 0$ mm corresponds to the start of the central part of the LCE balloon. A point $\mathbf{X}^{(3)}$ located on the outer surface at $z = 55.0$ mm is used to define a representative hoop stretch $\bar{\lambda}_\theta = r(\mathbf{X}^{(3)})/R_0$, where $R_0 = 5$ mm and $r(\cdot)$ is the evolving distance of a material point from the central axis.[1] For convenience in what follow, we refer to these quantities as the axial and hoop stretch, and we drop the over-bars.

4.3.1 Discussion of LCE balloon results

The computations were run dynamically using Newmark's method with $\beta = 1/4$, $\gamma = 1/2$ (second-order accurate in time with no numerical dissipation). Time-step size was dynamically controlled such that director rotation was targeted to be 0.7 degrees per time step using the algorithm of Weber et al. (1990). This is important for both reasonable accuracy but more importantly for stability of the non-linear iterations over the full computation. Helpful for these purposes is the fact that we have implemented the algorithmic tangent for or model's time integration, thereby providing for quadratic convergence of the global finite element problem at each time step.

Experimental data Shown in Fig. 13 by light colored markers are the experimental results of He et al. (2020), light blue for λ_θ versus pressure and light orange for λ_z versus pressure. Seen is an initial stiff response, λ_z and $\lambda_\theta \sim 1$, followed by a sudden jump of λ_θ to roughly $r^{1/2}$ and λ_z to roughly $r^{-1/2}$. With increasing pressure the balloon expands radially, while its length remains largely constant. Then at a critical pressure the balloon dramatically extends, from $\lambda_z \sim 0.45$ to $\lambda_z \sim 1.12$, along with a jump in λ_θ from about 3.9 to roughly 5.

[1] Radial distance r should not be confused with the anisotropy/step-length ratio r that is commonly used in the LCE literature. Context should make the distinction clear and thus we do not introduce additional notation in this context.

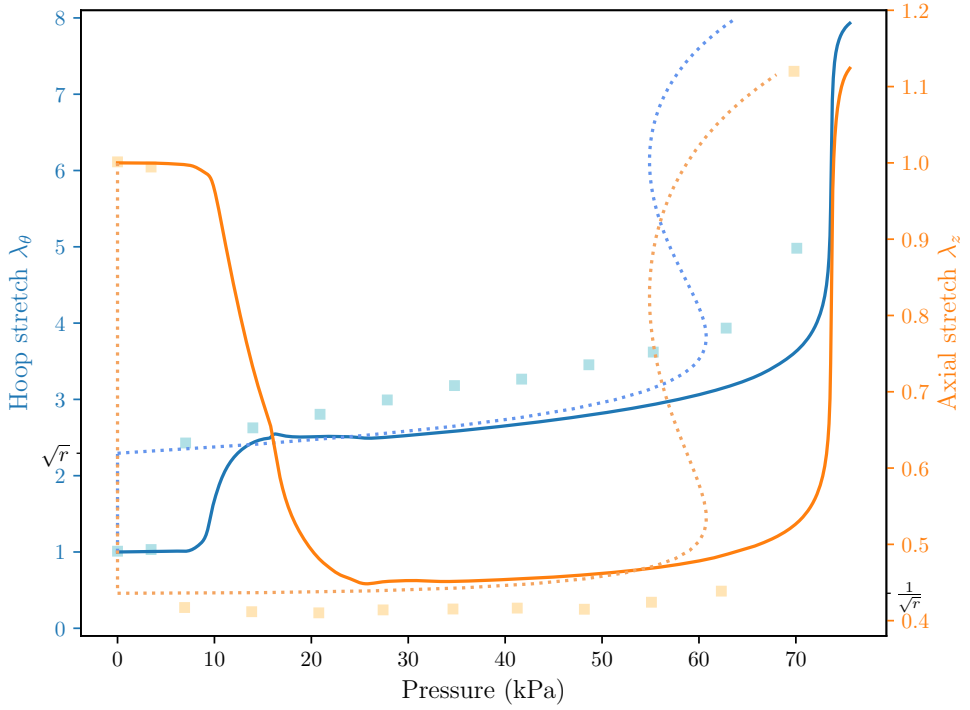

Figure 13: Pressure stretch response of LCE balloon. Measured data is given by the light colored markers, the dotted lines are the result of an idealized hand computation, the FEA computation is shown with solid lines. Blue correspond to the hoop response and Orange corresponds to the axial response.

Simple model Shown by the dotted lines in Fig. 13 is the prediction of a simple hand computation that assumes the balloon to be thin-walled, infinitely long, and governed by an incompressible *non-viscous* neo-Gent material. As a function of the hoop stretch one has that the hoop and axial Cauchy stresses are given by

$$\sigma_\theta = \begin{cases} 0 & \text{for } \lambda_\theta \in [0, \sqrt{r}] \\ J_m \mu_{eq} \dfrac{\lambda_\theta^2 r^{-1} - (\lambda_z \lambda_\theta)^{-2}}{3 + J_m - (\lambda_z \lambda_\theta)^{-2} - \lambda_\theta^2 r^{-1} - \lambda_z^2 r} & \text{for } \lambda_\theta > \sqrt{r}\,, \end{cases} \tag{42}$$

$$\sigma_z = \begin{cases} 0 & \text{for } \lambda_\theta \in [0, \sqrt{r}] \\ J_m \mu_{eq} \dfrac{\lambda_z^2 r - (\lambda_z \lambda_\theta)^{-2}}{3 + J_m - (\lambda_z \lambda_\theta)^{-2} - \lambda_\theta^2 r^{-1} - \lambda_z^2 r} & \text{for } \lambda_\theta > \sqrt{r}\,, \end{cases} \tag{43}$$

where the axial stretch in terms of the hoop stretch, for $\lambda_\theta > \sqrt{r}$, is given by

$$\lambda_z = \frac{1}{2r} \sqrt{\lambda_\theta^2 + \sqrt{\lambda_\theta^{-2}(\lambda_\theta^6 + 8r^3)}}\,. \tag{44}$$

The inflation pressure, P, can be found by noting

$$P = \frac{T_0 \sigma_\theta}{\bar{R} \lambda_\theta^2 \lambda_z}\,, \tag{45}$$

where $T_0 = 1$ mm is the initial thickness and $\bar{R} = 4.5$ mm is the mean initial radius.

In the simple model, there is first a radial jump at zero pressure due to a zero energy cost continuous director rotation from the axial direction to the tangential (hoop) direction. At each point along the jump the director rotates either $\pm$ some amount until the director orientations are fully in the tangential direction. At the same time there is an axial jump also due to the director rotations.

At higher pressures a limit point phenomena is seen just as is in balloon modeled with finite elasticity; see, e.g., Anand and Govindjee (2020a, §31.3) and Anand and Govindjee (2020b, §12.10). For continuously increasing pressure, the balloon would suddenly expand and lengthen at the limit point, something that is seen in the data. He et al. (2020) provide a similar solution using a neo-classical model. In that computation, increasing pressure "above" the limit point results in unbounded expansion of the balloon. With the neo-Gent model the material stiffens sufficiently to allow for increases above the limit point after a dynamic expansion process.

Neo-Gent ψ_{eq} FEA model Shown in Fig. 13 with solid lines is the prediction from our FEA model of the thick-walled finite length balloon. The model is noted to have a viscous director and a viscous network. Considering the coarse mesh and the lack of material parameter knowledge, the agreement with the data is quite good. We make the following observations:

1. The simulation picks up the initial very stiff balloon response seen in the experiment. The controlling element of the model here is the director viscosity which prevents the director from rotating instantly. The pressure at which the director rotation accelerates decreases with decreasing director viscosity and/or decreasing rate of change of pressure. If the pressure time history was known, this point could be used to determine the unknown director viscosity.

2. In the experiment, just above 60 kPa, a limit point was reached. Upon the next increase in the pressure, the balloon rapidly extended, going from a λ_z well below 1 to one of $\lambda_z > 1$. The FEA model is able to capture this feature due to the inclusion of inertia in the model. Barring the inclusion of dynamics, one would have to try to follow the quasi-static response seen in the simple non-viscous model. In a finite element computation, this would usually be achieved via the use of arc-length methods (see e.g., Wriggers, 2008, Chap. 5). However, for rate dependent models arc-length methods are not well established as one needs to control the "rate of loading" to have a specified value while simultaneously controlling the arc-length step size. The use of a dynamic computation allows us to avoid this complication at little computational cost. Note the Newmark time-stepping scheme we use is implicit and is greatly aided by our consistent tangent.

3. The rate of change of the pressure plays an important roll in the response. As noted already, it controls the pressure at which the director rotation begins to accelerate. But it also has an influence on the effective stiffness of the balloon. However, for the rates chosen in our example, this influence is not large.

4. It should be noted that in the computation, the *initial* director field is perturbed ± 1 degree from perfect alignment with the axis of the balloon. The plus/minus values alternate as one moves along the axis of the balloon. The result of this can be seen in Fig. 14 where the directors can be seen to stripe as the loading progresses. Without this type of perturbation it is possible for the directors to all rotate in the same direction. The resulting shears would induce gross rotation and twisting of the balloon. The alternating initial pattern allows for plus/minus cancellation of the cross-sectional rotations and provides for a basic model of microstructural striping in the balloon. This is consistent with the experiment (He et al., 2020, Figure 1) which showed the transparent balloon becoming opaque upon initial contraction (seen as alternating incomplete director rotations in our model), and then with further pressure becoming transparent (alignment in the tangential direction in our model). The evolution of this process from our model is seen by the director fields in Figs. 14-16.

5. As a last point we note that the data seems to indicate either that the value of r is actually greater than 5.26 and/or the equilibrium shear modulus of the material is less than 0.8 MPa at the start of the deformation. This follows from the fact that the data points lie outside of the $(r^{-1/2}, r^{1/2})$ interval. The finite length of the balloon and the possibility of viscous effects compound this issue. This points to the need for a more

sophisticated ψ_{eq} and, likely, ψ_{neq}.

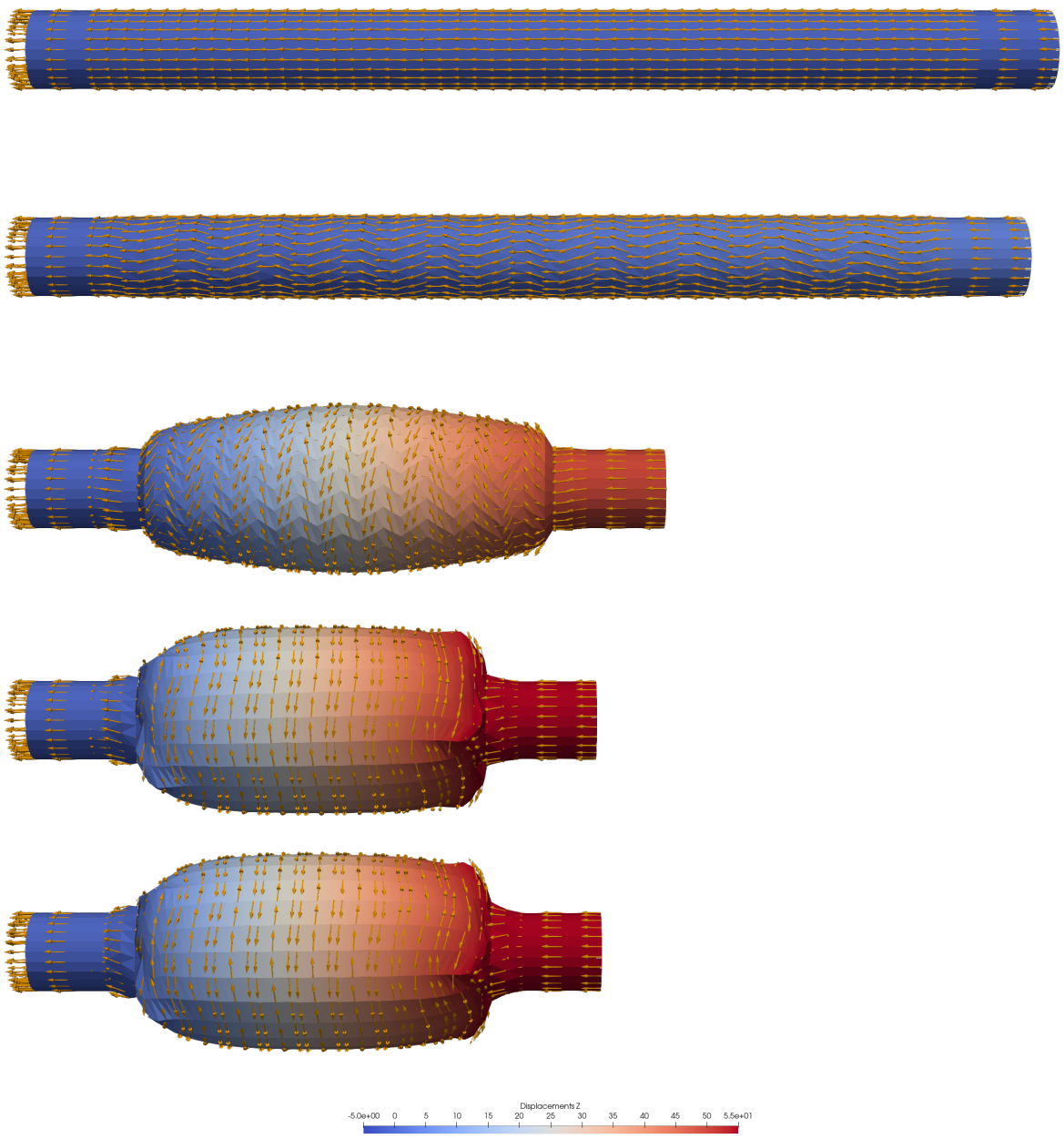

Figure 14: Snapshots of the (unscaled deformation) of the LCE balloon with director field and contours of axial motion at pressures of 0, 10, 20, 30, 40 kPa, top to bottom.

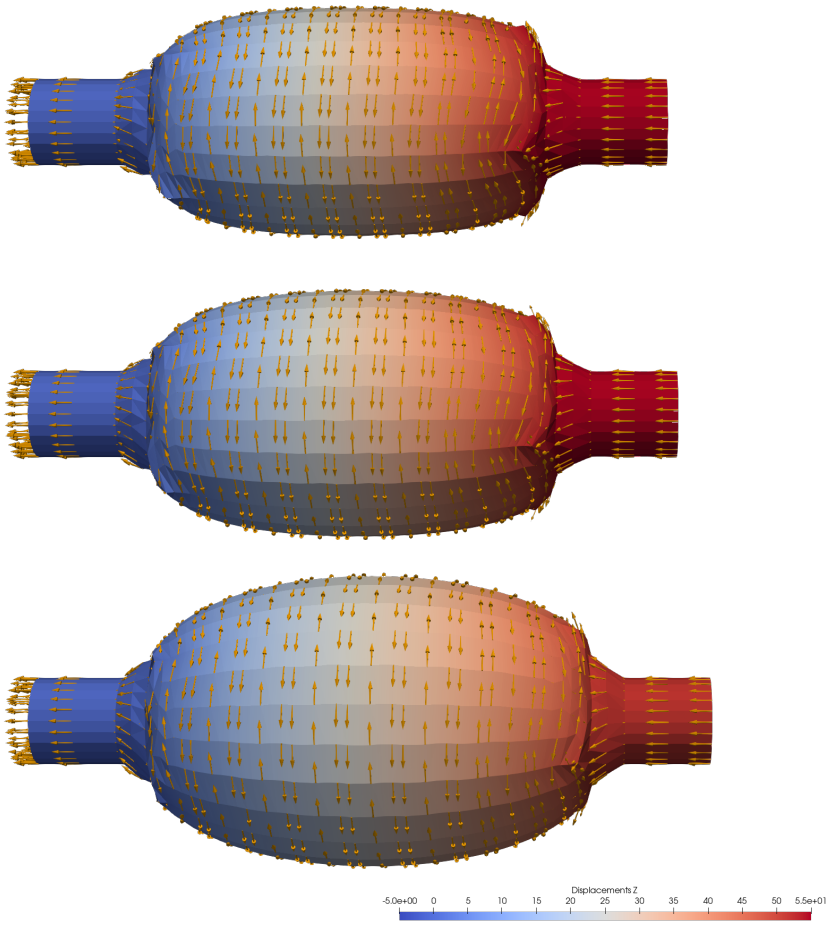

Figure 15: Snapshots of the (unscaled deformation) of the LCE balloon with director field and contours of axial motion at pressures of 50, 60, 70 kPa, top to bottom.

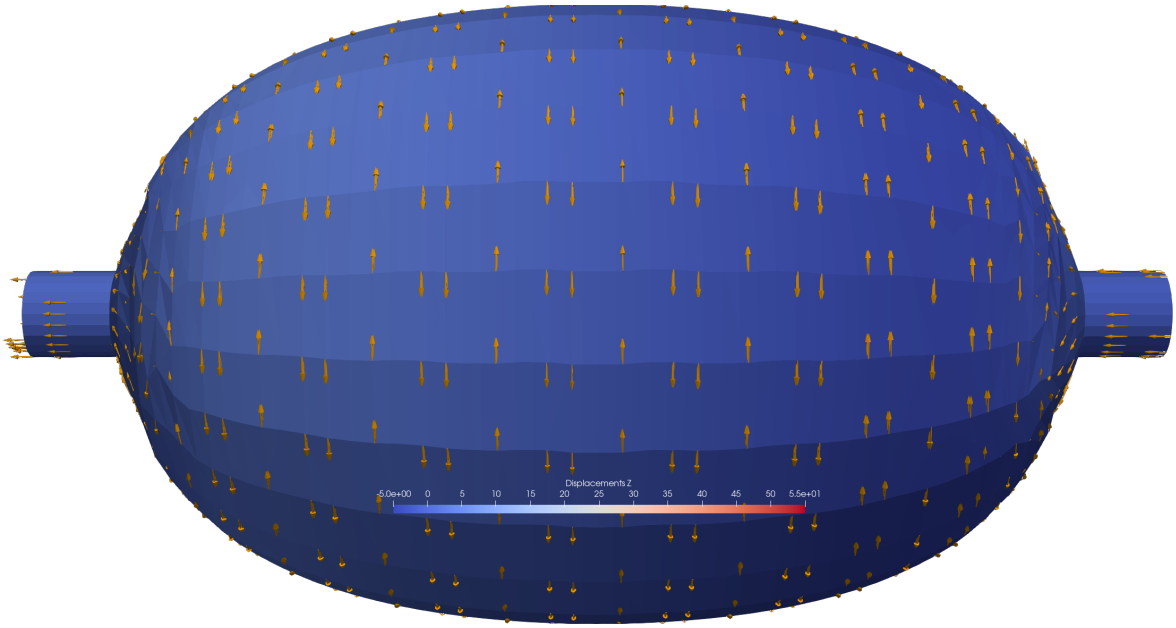

Figure 16: Snapshot of the (unscaled deformation) of the LCE balloon with director field and contours of axial motion at 75 kPa

5 Conclusion

In this work, we presented a framework for the simulation LCE mechanical boundary-value problems where the LCE is modeled as a viscoelastic media with a viscous director. We have detailed the best way to formulate the element residual and tangent, as well as the internal variables, for such models – including giving explicit expressions for the consistent tangent needed to achieve full quadratic convergence in nonlinear Newton iterations. For this class of materials, we also find that a first Piola-Kirchhoff implementation is most convenient since such LCE models require the use of the full deformation gradient and not just the right-stretch tensor. As such, a first Piola-Kirchhoff finite element implementation is the most efficient.

The framework developed was applied to three simulations which revealed important concepts with respect to the simulation of LCE systems. One concept is the importance of the careful specification of the initial director field in a material. The response is quite sensitive in certain situations and thus care must be exercised. The initial director field sensitivity also makes it necessary to look at boundary value problems, not just material point computations, since the initial director field (a feature that is unavailable when looking at a material point alone) plays a big role in the experimental and theoretical response of these materials. A secondary, related finding is that assumptions from material point computations can lead to incorrect results when boundary value problems are solved. Third, we find that the proper modeling of LCEs appears to require the use of nonlinear (deformation/load dependent) director viscosities in addition to network viscoelasticity for compression. How-

ever, in tension we find that a constant director viscosity is adequate in contrast to what has been inferred from material point computations in the past. The characterization of these viscosity functions is an open question deserving of further study. Lastly, we have shown using the balloon example of He et al. (2020) that the model of Wang et al. (2022) has the ability to model quite complex LCE response.

Acknowledgments

AEHC acknowledges the support of a Margaret and T.Y. Lin graduate fellowship. SG acknowledges support via a Humboldt Research Award for the completion of this work. TDN and BS acknowledges support from the the Army Research Lab (W911NF2220068).

References

V. Agostiniani and A. DeSimone. Ogden-type energies for nematic elastomers. *International Journal of Non-Linear Mechanics*, 47:402–412, 2012.

J. Ahrens, B. Geveci, and C. Law. *ParaView: An End-User Tool for Large Data Visualization, Visualization Handbook*. Elsevier, 2005.

L. Anand and S. Govindjee. *Continuum Mechanics of Solids*. Oxford University Press, 2020a.

L. Anand and S. Govindjee. *Example Problems for Continuum Mechanics of Solids*. 2020b.

A. Azoug, V. Vasconcellos, J. Dooling, M. Saed, C.M. Yakacki, and T.D. Nguyen. Viscoelasticity of the polydomain-monodomain transition in main-chain liquid crystal elastomers. *Polymer (Guildf).*, 98:165–171, 2016.

P. Bladon, E. M. Terentjev, and M. Warner. Transitions and instabilities in liquid-crystal elastomers. *Physical Review E*, 47:3838–3840, 1993.

S. Conti, A. DeSimone, and G. Dolzmann. Soft elastic response of stretched sheets of nematic elastomers: a numerical study. *Journal of the Mechanics and Physics of Solids*, 50:1431–1451, 2002.

B. Dacorogna. *Direct Methods in the Calculus of Variations*. Springer, 2008.

A. DeSimone and G. Dolzmann. Macroscopic response of nematic elastomers via relaxation of a class of so(3)-invariant energies. *Archive for Rational Mechanics and Analysis*, 161: 181–204, 2002.

A. DeSimone and L. Teresi. Elastic energies for nematic elastomers. *The European Physical Journal E*, 29:191–204, 2009.

E. Fried and S. Sellers. Free-energy density functions for nematic elastomers. *Journal of the Mechanics and Physics of Solids*, 52:1671–1689, 2004.

R.J. Gaylord. A theory of the stress-induced crystallization of crosslinked polymeric networks. *Journal of Polymer Science. Part B, Polymer Physics*, 14:1827–1837, 1976.

R.J. Gaylord and D.J. Lohse. Morphological changes during oriented polymer crystallization. *Polymer Engineering and Science*, 16:163–167, 1976.

A.N. Gent. Crystallization and the relaxation of stress in stretched natural rubber vulcanizates. *Transactions of the Faraday Society*, 50:521–533, 1954.

Q. He, Y. Zheng, Z. Wang, X. He, and S. Cai. Anomalous inflation of a nematic balloon. *Journal of the Mechanics and Physics of Solids*, 142:104013, 2020.

I. Kundler and H. Finkelmann. Strain-induced director reorientation in nematic liquid single crystal elastomers. *Macromolecular Rapid Communications*, 16:637–704, 1995.

V. Lee, A. Wihardja, and K. Bhattacharya. A macroscopic constitutive relation for isotropic-genesis, polydomain liquid crystal elastomers. 2023. URL http://arxiv.org/abs/2303.14783v1.

C.P.M. Linares, N.A. Traugutt, M.O. Saed, A.M. Linares, C.M. Yakacki, and T.D. Nguyen. The effect of alignment on the rate-dependent behavior of a main-chain liquid crystal elastomer. *Soft Matter*, 16:8782–8798, 2020.

S.J. Mistry and S. Govindjee. A micro-mechanically based continuum model for strain-induced crystallization in natural rubber. *International Journal of Solids and Structures*, pages 530–539, 2014.

M.O. Saed, A.H. Torbati, C.A. Starr, R. Visvanathan, N.A. Clark, and C.M. Yakacki. Thiol-acrylate main-chain liquidcrystalline elastomers with tunable thermomechanical properties and actuation strain. *Journal of Polymer Science, Part B: Polymer Physics*, 55:157–168, 2017.

F. Sidoroff. Un modèle viscoélastique non linéaire avec configuration intermédiaire. *Journal de Mécanique*, 13:679–713, 1974.

A. Sonnet and E. Virga. *Dissipative Ordered Fluids*. Springer, 2012.

R.L. Taylor and S. Govindjee. *FEAP - A Finite Element Analysis Program, User Manual*. University of California, Berkeley, 2020. URL http://projects.ce.berkeley.edu/feap.

S. Toki, I. Sics, B.S. Hsiao, M. Tosaka, S. Poompradub, Y. Ikeda, and S. Kohjiya. Probing the nature of strain-induced crystallization in polyisoprene rubber by combined thermo-mechanical and in situ x-ray diffraction techniques. *Macromolecules*, 38:7064–7073, 2005.

Z. Wang, A. E. H. Chehade, S. Govindjee, and T. Nguyen. A nonlinear viscoelastic theory for nematic liquid crystal elastomers. *Journal of the Mechanics and Physics of Solids*, 163, 2022.

M. Warner and E. Terentjev. *Liquid Crystal Elastomers*. Oxford University Press, 2003.

G.G. Weber, A.M. Lush, A. Zavaliangos, and L. Anand. An objective time-integration procedure for isotropic rate-independent and rate-dependent elastic-plastic constitutive equations. *International Journal of Plasticity*, 6:701–744, 1990.

P. Wriggers. *Nonlinear Finite Element Methods*. Springer Berlin Heidelberg, Berlin, Heidelberg, 2008.

C. M. Yakacki, M. Saed, D. P. Nair, T. Gong, S. M. Reed, and C. N. Bowman. Tailorable and programmable liquid-crystalline elastomers using a two-stage thiol-acrylate reaction. *Royal Society of Chemistry Advances*, 5:18997–19001, 2015.

Y. Zhang, C. Xuan, Y. Jiang, and Y. Huo. Continuum mechanical modeling of liquid crystal elastomers as dissipative ordered solids. *Journal of the Mechanics and Physics of Solids*, 126:285–303, 2019.

O.C. Zienkiewicz, R.L. Taylor, and J.Z. Zhu. *The Finite Element Method: its Basis and Fundamentals (Seventh Edition)*. Butterworth-Heinemann, Oxford, seventh edition edition, 2013.

O.C. Zienkiewicz, R.L. Taylor, and D.D. Fox. *The Finite Element Method for Solid and Structural Mechanics (Seventh Edition)*. Butterworth-Heinemann, Oxford, seventh edition edition, 2014.

A Tensor vector-matrix maps

In solving for the incremental evolution of the internal variables, it is convenient to define a tensor-to-vector operator:

$$(\mathbf{F})_{vec} = \begin{bmatrix} \mathrm{F}_{11} \\ \mathrm{F}_{21} \\ \mathrm{F}_{31} \\ \mathrm{F}_{12} \\ \mathrm{F}_{22} \\ \mathrm{F}_{32} \\ \mathrm{F}_{13} \\ \mathrm{F}_{23} \\ \mathrm{F}_{33} \end{bmatrix} . \tag{46}$$

The internal variables to be solved for at Gauss points are rearranged into a vector $\boldsymbol{x} \in \mathbb{R}^{24}$:

$$\boldsymbol{x} = \begin{bmatrix} (\mathbf{F}^v)_{vec} \\ (\mathbf{F}^e)_{vec} \\ \hat{\boldsymbol{d}} \\ \boldsymbol{d} \end{bmatrix} . \tag{47}$$

When computing, we map 4th order tensors to 9×9 matrices:

$$(\mathcal{A})_{9\times 9} = \begin{bmatrix} \mathcal{A}_{1111} & \mathcal{A}_{1121} & \mathcal{A}_{1131} & \mathcal{A}_{1112} & \mathcal{A}_{1122} & \mathcal{A}_{1132} & \mathcal{A}_{1113} & \mathcal{A}_{1123} & \mathcal{A}_{1133} \\ \mathcal{A}_{2111} & \mathcal{A}_{2121} & \mathcal{A}_{2131} & \mathcal{A}_{2112} & \mathcal{A}_{2122} & \mathcal{A}_{2132} & \mathcal{A}_{2113} & \mathcal{A}_{2123} & \mathcal{A}_{2133} \\ \mathcal{A}_{3111} & \mathcal{A}_{3121} & \mathcal{A}_{3131} & \mathcal{A}_{3112} & \mathcal{A}_{3122} & \mathcal{A}_{3132} & \mathcal{A}_{3113} & \mathcal{A}_{3123} & \mathcal{A}_{3133} \\ \mathcal{A}_{1211} & \mathcal{A}_{1221} & \mathcal{A}_{1231} & \mathcal{A}_{1212} & \mathcal{A}_{1222} & \mathcal{A}_{1232} & \mathcal{A}_{1213} & \mathcal{A}_{1223} & \mathcal{A}_{1233} \\ \mathcal{A}_{2211} & \mathcal{A}_{2221} & \mathcal{A}_{2231} & \mathcal{A}_{2212} & \mathcal{A}_{2222} & \mathcal{A}_{2232} & \mathcal{A}_{2213} & \mathcal{A}_{2223} & \mathcal{A}_{2233} \\ \mathcal{A}_{3211} & \mathcal{A}_{3221} & \mathcal{A}_{3231} & \mathcal{A}_{3212} & \mathcal{A}_{3222} & \mathcal{A}_{3232} & \mathcal{A}_{3213} & \mathcal{A}_{3223} & \mathcal{A}_{3233} \\ \mathcal{A}_{1311} & \mathcal{A}_{1321} & \mathcal{A}_{1331} & \mathcal{A}_{1312} & \mathcal{A}_{1322} & \mathcal{A}_{1332} & \mathcal{A}_{1313} & \mathcal{A}_{1323} & \mathcal{A}_{1333} \\ \mathcal{A}_{2311} & \mathcal{A}_{2321} & \mathcal{A}_{2331} & \mathcal{A}_{2312} & \mathcal{A}_{2322} & \mathcal{A}_{2332} & \mathcal{A}_{2313} & \mathcal{A}_{2323} & \mathcal{A}_{2333} \\ \mathcal{A}_{3311} & \mathcal{A}_{3321} & \mathcal{A}_{3331} & \mathcal{A}_{3312} & \mathcal{A}_{3322} & \mathcal{A}_{3332} & \mathcal{A}_{3313} & \mathcal{A}_{3323} & \mathcal{A}_{3333} \end{bmatrix} , \tag{48}$$

Third order tensors are mapped to 3×9 and 9×3 matrices depending upon if they appear

as maps from vectors to tensors or vice-versa:

$$(\mathcal{M})_{9\times 3} = \begin{bmatrix} \mathcal{M}_{111} & \mathcal{M}_{112} & \mathcal{M}_{113} \\ \mathcal{M}_{211} & \mathcal{M}_{212} & \mathcal{M}_{213} \\ \mathcal{M}_{311} & \mathcal{M}_{312} & \mathcal{M}_{313} \\ \mathcal{M}_{121} & \mathcal{M}_{122} & \mathcal{M}_{123} \\ \mathcal{M}_{221} & \mathcal{M}_{222} & \mathcal{M}_{223} \\ \mathcal{M}_{321} & \mathcal{M}_{322} & \mathcal{M}_{323} \\ \mathcal{M}_{131} & \mathcal{M}_{132} & \mathcal{M}_{133} \\ \mathcal{M}_{231} & \mathcal{M}_{232} & \mathcal{M}_{233} \\ \mathcal{M}_{331} & \mathcal{M}_{332} & \mathcal{M}_{333} \end{bmatrix} , \tag{49}$$

$$(\mathcal{M})_{3\times 9} = \begin{bmatrix} \mathcal{M}_{111} & \mathcal{M}_{121} & \mathcal{M}_{131} & \mathcal{M}_{112} & \mathcal{M}_{122} & \mathcal{M}_{132} & \mathcal{M}_{113} & \mathcal{M}_{123} & \mathcal{M}_{133} \\ \mathcal{M}_{211} & \mathcal{M}_{221} & \mathcal{M}_{231} & \mathcal{M}_{212} & \mathcal{M}_{222} & \mathcal{M}_{232} & \mathcal{M}_{213} & \mathcal{M}_{223} & \mathcal{M}_{233} \\ \mathcal{M}_{311} & \mathcal{M}_{321} & \mathcal{M}_{331} & \mathcal{M}_{312} & \mathcal{M}_{322} & \mathcal{M}_{332} & \mathcal{M}_{313} & \mathcal{M}_{323} & \mathcal{M}_{333} \end{bmatrix} . \tag{50}$$

Observe that these last two mappings are not transposes of each other.

B Tangent terms

B.1 Tangent terms for Gauss point iterations

The free energy derivatives used for the evolution of the internal variables and the residual and tangent computations are written compactly as:

$$\mathbf{Q} = \frac{\partial \Psi_{eq}}{\partial \mathbf{F}} \left(\mathbf{F}_{n+1}, \boldsymbol{d}_{n+1} \right) , \qquad \mathbf{Q}^e = \frac{\partial \Psi_{neq}}{\partial \mathbf{F}^e} \left(\mathbf{F}^e, \boldsymbol{d} \right) , \tag{51}$$

$$\mathcal{A} = \frac{\partial^2 \Psi_{eq}}{\partial \mathbf{F} \otimes \partial \mathbf{F}} \left(\mathbf{F}_{n+1}, \boldsymbol{d}_{n+1} \right) , \qquad \mathcal{A}^e = \frac{\partial^2 \Psi_{neq}}{\partial \mathbf{F}^e \otimes \partial \mathbf{F}^e} \left(\mathbf{F}^e, \boldsymbol{d} \right) , \tag{52}$$

$$\mathcal{M} = \frac{\partial^2 \Psi_{eq}}{\partial \mathbf{F} \otimes \partial \boldsymbol{d}} \left(\mathbf{F}_{n+1}, \boldsymbol{d}_{n+1} \right) , \qquad \mathcal{M}^e = \frac{\partial^2 \Psi_{neq}}{\partial \mathbf{F}^e \otimes \partial \boldsymbol{d}} \left(\mathbf{F}^e, \boldsymbol{d} \right) , \tag{53}$$

$$\boldsymbol{h} = \frac{\partial \Psi}{\partial \boldsymbol{d}} \left(\mathbf{F}, \mathbf{F}^e, \boldsymbol{d} \right) , \qquad \mathcal{D} = \frac{\partial^2 \Psi}{\partial \boldsymbol{d} \otimes \partial \boldsymbol{d}} \left(\mathbf{F}, \mathbf{F}^e, \boldsymbol{d} \right) . \tag{54}$$

Using these definitions the entries of the local Gauss point tangent matrix are given by:

$$\left[\frac{\partial \mathbf{G}_1 \left(\mathbf{F}^v, \mathbf{F}^e, \boldsymbol{d} \right)}{\partial \mathbf{F}^v} \right]_{\alpha A \beta B} = \left[\mathbf{1} - \frac{\Delta t_n}{\eta_N} \left(\mathbf{F}^e \right)^\top \mathbf{Q}^e \right]_{\alpha\beta} \delta_{AB} , \tag{55}$$

$$\left[\frac{\partial \mathbf{G}_1 \left(\mathbf{F}^v, \mathbf{F}^e, \boldsymbol{d} \right)}{\partial \mathbf{F}^e} \right]_{\alpha A i \beta} = -\frac{\Delta t_n}{\eta_N} \left(\delta_{\alpha\beta} \left[\mathbf{Q}^e \mathbf{F}^v \right]_{iA} + \left(\mathbf{F}^e \right)_{k\alpha} \left(\mathcal{A}^e \right)_{k\gamma i \beta} \left(\mathbf{F}^v \right)_{\gamma A} \right) , \tag{56}$$

$$\left[\frac{\partial \mathbf{G}_1 \left(\mathbf{F}^v, \mathbf{F}^e, \boldsymbol{d} \right)}{\partial \boldsymbol{d}} \right]_{\alpha A i} = -\frac{\Delta t_n}{\eta_N} \left(\mathbf{F}^e \right)_{k\alpha} \left(\mathcal{M}^e \right)_{k\gamma i} \left(\mathbf{F}^v \right)_{\gamma A} , \tag{57}$$

$$\left[\frac{\partial \mathbf{G}_2\left(\mathbf{F}^v, \mathbf{F}^e; \mathbf{F}\right)}{\partial \mathbf{F}^v}\right]_{iA\beta B} = -\left(\mathbf{F}^e\right)_{i\beta}\delta_{AB}\,, \tag{58}$$

$$\left[\frac{\partial \mathbf{G}_2\left(\mathbf{F}^v, \mathbf{F}^e; \mathbf{F}\right)}{\partial \mathbf{F}^e}\right]_{iAj\beta} = -\delta_{ij}\left(\mathbf{F}^v\right)_{\beta A}\,, \tag{59}$$

$$\left[\frac{\partial \boldsymbol{g}_3\left(\mathbf{F}^e, \hat{\boldsymbol{d}}, \boldsymbol{d}; \mathbf{F}\right)}{\partial \mathbf{F}^e}\right]_{ij\alpha} = \frac{\Delta t_n}{\eta_D}\left(\mathbf{1} - \boldsymbol{d}\otimes\boldsymbol{d}\right)_{ik}\left(\mathcal{M}^e\right)_{j\alpha k}\,, \tag{60}$$

$$\frac{\partial \boldsymbol{g}_3\left(\mathbf{F}^e, \hat{\boldsymbol{d}}, \boldsymbol{d}; \mathbf{F}\right)}{\partial \hat{\boldsymbol{d}}} = \mathbf{1}\,, \tag{61}$$

$$\frac{\partial \boldsymbol{g}_3\left(\mathbf{F}^e, \hat{\boldsymbol{d}}, \boldsymbol{d}; \mathbf{F}\right)}{\partial \boldsymbol{d}} = -\Delta t_n \mathbf{W} + \frac{\Delta t_n}{\eta_D}\left[\left(\mathbf{1} - \boldsymbol{d}\otimes\boldsymbol{d}\right)\mathcal{D} - \boldsymbol{d}\otimes\boldsymbol{h} - \left(\boldsymbol{d}\cdot\boldsymbol{h}\right)\mathbf{1}\right]\,, \tag{62}$$

$$\frac{\partial \boldsymbol{g}_4\left(\hat{\boldsymbol{d}}, \boldsymbol{d}\right)}{\partial \hat{\boldsymbol{d}}} = \mathbf{1} - \frac{1}{\left\|\hat{\boldsymbol{d}}\right\|}\boldsymbol{d}\otimes\hat{\boldsymbol{d}}\,, \tag{63}$$

$$\left[\frac{\partial \boldsymbol{g}_4\left(\hat{\boldsymbol{d}}, \boldsymbol{d}\right)}{\partial \boldsymbol{d}}\right]_{ij} = -\left\|\hat{\boldsymbol{d}}\right\|\mathbf{1}\,. \tag{64}$$

B.2 Expressions needed for element tangent

The computation of the element tangent requires the derivatives of the Gauss point residual with respect to the deformation gradient:

$$\left(\frac{\partial \boldsymbol{g}}{\partial \mathbf{F}}\right)_{24\times 9} = \left(\mathbf{0}_{9\times 9}, \quad \left(\frac{\partial \mathbf{G}_2}{\partial \mathbf{F}}_{\,9\times 9}\right)^{\top}, \quad \left(\frac{\partial \boldsymbol{g}_3}{\partial \mathbf{F}}_{\,3\times 9}\right)^{\top}, \quad \mathbf{0}_{9\times 3}^{\top}\right)^{\top}. \tag{65}$$

The partial derivatives in 65 are given as:

$$\left[\frac{\partial \mathbf{G}_2\left(\mathbf{F}^v, \mathbf{F}^e; \mathbf{F}\right)}{\partial \mathbf{F}}\right]_{iAjB} = \delta_{ij}\delta_{AB}\,, \tag{66}$$

$$\left[\frac{\partial \boldsymbol{g}_3\left(\mathbf{F}^e, \hat{\boldsymbol{d}}, \boldsymbol{d}; \mathbf{F}\right)}{\partial \mathbf{F}}\right]_{ijA} = -\left[\frac{\partial \Delta t_n \mathbf{W}}{\partial \mathbf{F}}\right]_{ikjA} d_k + \frac{\Delta t_n}{\eta_D}\left(\mathbf{1} - \boldsymbol{d}\otimes\boldsymbol{d}\right)_{ik}\left(\mathcal{M}\right)_{j\alpha k}\,, \tag{67}$$

where

$$\left[\frac{\partial \Delta t_n \mathbf{W}}{\partial \mathbf{F}}\right]_{ikjA} = \left(\mathbf{F}_n\mathbf{F}^{-1}\right)_{ij}\left(\mathbf{F}^{-1}\right)_{Ak} - \left(\mathbf{F}_n\mathbf{F}^{-1}\right)_{kj}\left(\mathbf{F}^{-1}\right)_{Ai}\,. \tag{68}$$

C Traditional Stress Divergence Forms

The weak form relations are often expressed in the current configuration and take advantage of tensor symmetries, as well as underlying hyperelastic formulation foundations. In these settings, the internal work contribution to the weak form, the first variation, is given as

$$\int_{\mathcal{B}} P_{iA}\delta\varphi_{i,A}\,dV\,, \tag{69}$$

equivalently

$$\int_{\boldsymbol{\varphi}(\mathcal{B})} \frac{1}{J}\tau_{ij}\delta\varphi_{i,j}\,dv\,, \tag{70}$$

where we adopt the standard convention of upper and lower case indices to distinguish spatial and referential derivatives and $\boldsymbol{\tau} = \mathbf{P}\mathbf{F}^{\mathsf{T}}$ is the Kirchhoff stress. Observe that to compute $\boldsymbol{\tau}$ for an LCE, one *must* first compute $\mathbf{P}$. The computation of $\boldsymbol{\tau}$ is simply unneeded extra work.

The second variation when utilizing (69) is

$$\int_{\mathcal{B}} \delta\varphi_{i,A}\mathcal{A}_{iAjB}\Delta\varphi_{j,B}\,dV\,, \tag{71}$$

where the moduli $\mathcal{A}_{iAjB} = [\Delta P_{iA}]_{jB}$ are the tangent moduli, the variation of the stress with respect to the motion. When using (70) and following the traditional formulation one has for the second variation

$$\int_{\boldsymbol{\varphi}(\mathcal{B})} \frac{1}{J}\delta\varphi_{i,j}[\delta_{ik}\tau_{jl} + c_{ijkl}]\Delta\varphi_{k,l}\,dv\,, \tag{72}$$

where the first term is the geometric tangent and the second term is the consistent material tangent. In the case of LCEs, to compute the material tangent term, on must first compute $\mathcal{A}_{iAjB}$; it is not possible to directly compute c_{ijkl} as, say, in a conventional material, and from there one must perform the extra computation

$$c_{ijkl} = -\delta_{ij}\tau_{jl} + \mathcal{A}_{iAkB}F_{jA}F_{lB}\,. \tag{73}$$

For the case of LCEs, this extra work provides no computational advantage since c_{ijkl} only possesses minor symmetries. In particular, it does not possess major symmetries. These observations hold for LCEs with or without viscous and/or viscoelastic properties.